HHS Public Access

Author manuscript

Dev Cell. Author manuscript; available in PMC 2025 January 22.

Published in final edited form as:

Dev Cell. 2024 January 22; 59(2): 199–210.e11. doi:10.1016/j.devcel.2023.12.001.

MAP9/MAPH-9 supports axonemal microtubule doublets and modulates motor movement

Michael V. Tran[1], **Daria Khuntsariya**[2], **Richard D. Fetter**[3], **James W. Ferguson**[1], **Jennifer T. Wang**[1], **Alexandra F. Long**[1], **Lauren E. Cote**[1], **Stephen R. Wellard**[1], **Nabor Vázquez-Martínez**[1], **Maria D. Sallee**[1], **Mariya Genova**[4,5], **Maria M. Magiera**[4,5], **Sani Eskinazi**[1], **Jessica D. Lee**[6], **Nina Peel**[6], **Carsten Janke**[4,5], **Tim Stearns**[1,7], **Kang Shen**[3], **Zdenek Lansky**[2], **Jérémy Magescas**[1,*], **Jessica L. Feldman**[1,8,*]

[1]Department of Biology, Stanford University, Stanford, CA 94305, USA.

[2]Institute of Biotechnology, Czech Academy of Sciences, BIOCEV, 25250 Vestec, Prague West, Czech Republic.

[3]Howard Hughes Medical Institute, Department of Biology, Stanford University, Stanford, CA 94305, USA.

[4]Institut Curie, Université PSL, CNRS UMR3348, Orsay, France.

[5]Université Paris-Saclay, CNRS UMR3348, Orsay, France.

[6]The College of New Jersey, Ewing, NJ 08628, USA.

[7]Department of Genetics, Stanford University School of Medicine, Stanford, CA 94305, USA.

[8]Lead Contact

Summary:

*Correspondence: jmagesca@stanford.edu, feldmanj@stanford.edu.

Author Contributions

Conceptualization: M.V.T; J.M.; J.L.F.

Investigation: M.V.T; J.M.; N.V.M.; J.W.F.; S.R.W.; R.D.F; A.F.L; J.T.W.; M.G.; M.M.M; C.J.; D.K.; Z.L; M.D.S.; L.E.C.; S.E.; J.D.L.; N.P.

Formal Analysis: M.V.T; J.M.; L.E.C.

Resources: J.L.F.; T.S.; K.S.; C.J.; Z.L.

Writing – Original Draft: M.V.T; J.L.F.

Review & Editing: M.V.T; J.L.F.; J.M.

Visualization: M.V.T; J.M.; J.W.F. L.E.C. J.L.F.

Supervision: J.L.F.; J.M.

Declaration of Interests None.

Inclusion and Diversity:

We worked to ensure sex balance in the selection of non-human subjects and diversity in experimental samples through the selection of the cell lines and/or of genomic datasets. One or more of the authors of this paper self-identifies as an ethnic minority in their field of research or within their geographical location, as a gender minority in their field of research, and/or as a member of the LGBTQIA+ community. We avoided "helicopter science" practices by including the participating local contributors from the region where we conducted the research as authors on the paper.

Microtubule doublets (MTDs) comprise an incomplete microtubule (B-tubule) attached to the side of a complete cylindrical microtubule. These compound microtubules are conserved in cilia across the tree of life, however the mechanisms by which MTDs form and are maintained *in vivo* remain poorly understood. Here, we identify microtubule-associated protein 9 (MAP9) as a MTD-associated protein. We demonstrate that *C. elegans* MAPH-9, a MAP9 homolog, is present during MTD assembly and localizes exclusively to MTDs, a preference that is in part mediated by tubulin polyglutamylation. Loss of MAPH-9 caused ultrastructural MTD defects, including shortened, and/or squashed B-tubules with reduced numbers of protofilaments, dysregulated axonemal motor velocity, and perturbed cilia function. As we found that the mammalian ortholog MAP9 localized to axonemes in cultured mammalian cells and mouse tissues, we propose that MAP9/MAPH-9 plays a conserved role in regulating ciliary motors and supporting the structure of axonemal MTDs.

eTOC Blurb

Tran et al. identify a role for the microtubule associated protein MAP9/MAPH-9 in cilia, specialized cellular appendages composed of microtubule doublets. They discover that *C. elegans* MAPH-9 localizes exclusively to microtubule doublets, shaping doublet architecture and enabling cilia function. Mammalian MAP9 also localized to cilia, suggesting a conserved role.

Graphical Abstract

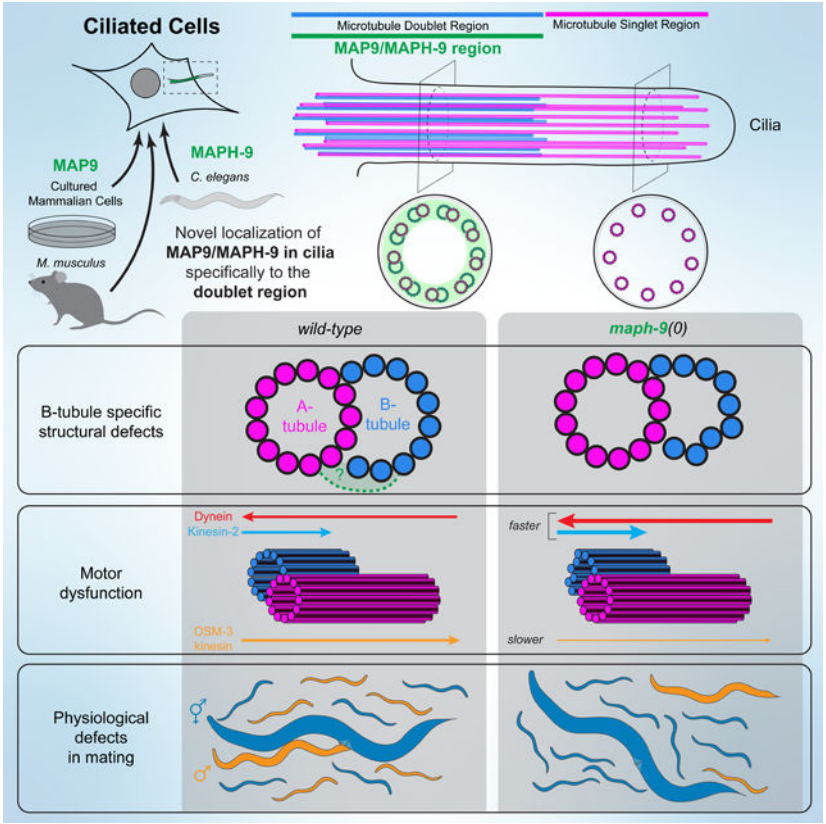

Introduction:

Microtubules are essential intracellular polymers made of α- and β-tubulin heterodimers stacked end-to-end to build laterally-associated protofilaments that form a hollow cylinder. However, in specialized cellular appendages called cilia, microtubules are instead found in figure-8 microtubule doublets (MTDs) composed of a single microtubule made of 13 protofilaments (the A-tubule) attached to an incomplete microtubule made of 10 protofilaments (the B-tubule) (Figure 1B). Most cilia have nine MTDs arranged with radial symmetry to form the axoneme, which provides the tracks for molecular motors to transport cargo through intraflagellar transport (IFT) to build and maintain cilia and support their function.

MTD formation *in vitro* can be driven by subtilisin treatment which cleaves the C-terminal tails from α- and β-tubulin[1]. *in vivo,* MTD formation is poorly understood, with loss of a handful of components leading to MTD defects: the microtubule inner protein FAP52, the inner junction protein FAP20, centriole components δ-tubulin, ε-tubulin, and HYLS-1, or the ciliary membrane-associated G-protein ARL13B[2–13]. However, some of these components are not conserved and/or likely impact MTD formation indirectly.

The identity and role of lattice binding microtubule-associated proteins (MAPs) at MTDs remain largely unknown[14,15]. Although originally shown to localize to cytoplasmic microtubules and play roles in the mitotic spindle[16], MAP9/ASAP has been implicated in cilia-related processes: a *MAP9* deletion enhances retinal degeneration in miniature long-haired dachshunds caused by an insertion in the gene for ciliary protein RPGRIP1[17]; Map9 depletion in zebrafish causes developmental defects associated with dysregulation of cilia-based hedgehog signaling[18]; MAP9 was found in the mouse photoreceptor sensory cilium proteome[19]; and the *C. elegans* homolog MAPH-9 is expressed in ciliated sensory neurons and localizes to cilia when overexpressed[20,21]. Despite this evidence, MAP9 function within cilia has been unexplored.

We used *C. elegans* to determine the *in vivo* function of MAP9, finding a role for MAPH-9 specifically in cilia. Endogenous MAPH-9 localized exclusively to axonemal MTDs, distinguishing these structures in part through a preference for polyglutamylated tubulin. Although cilia were present in *maph-9* deletion mutants, the velocity and frequency of IFT motors were affected and the anterograde motor OSM-3 had functional defects. Furthermore, we found a role for MAPH-9 in building and/or maintaining MTDs as *maph-9* mutants had defects in B-tubule shape and protofilament number and MTDs terminated prematurely in a subset of axonemes. These defects had physiological consequences as *maph-9* mutants had defects in mating, a process which relies on cilia. Finally, we found that MAP9 localization is conserved in mammalian motile and primary cilia, thus our work identifies a role for an understudied MAP in shaping and supporting MTDs.

Results:

MAPH-9 localizes to the microtubule doublet region of the axoneme

We explored the endogenous localization pattern of MAPH-9 in *C. elegans* by inserting GFP (green fluorescent protein) into the endogenous *maph-9* locus using CRISPR/Cas9. Live imaging in young adult worms showed that GFP::MAPH-9 is exclusively expressed in all ciliated cells, which in *C. elegans* is a subset of sensory neurons that include groups in the head (amphids) and the tail (phasmids)(Figure 1A and Figure S1A, S1B). MAPH-9 colocalized with endogenously tagged β-tubulin/TBB-4::RFP, a cilia-specific tubulin isotype that localizes to the whole ciliary axoneme, but was enriched distally[22,23], and RFP::SPD-5, the functional homolog of CDK5RAP2, which marks the base of cilia (Figure 1A)[24,25]. Intriguingly, although MAPH-9 localized to all cilia, its localization was restricted to the proximal region of the axoneme. We compared the length of MAPH-9 localization to the endogenously tagged dynein component D2LIC/XBX-1::RFP which localizes along the length of each cilium (Figure 1C and 1D). MAPH-9 localization was significantly shorter than that of XBX-1 (Figure 1D) and notably similar to the MTD region of the axoneme (so-called middle segment in *C. elegans* cilia) as measured from serial electron microscopy (EM) reconstruction (Figure 1B-D)[26,27]. To confirm the link between MAPH-9 and MTDs, we compared the localization of MAPH-9 to that of endogenous ARL-13 which localizes to the region of the ciliary membrane adjacent to MTDs past the transition zone[28–30] and found that MAPH-9 and ARL-13 extend to the same distal region within cilia (Figure S1C and S1D). While their distal localization was shared, MAPH-9 localized more proximally than ARL-13, coincident with the MTDs found at the base of cilia. Together, these data strongly suggest that MAPH-9 localizes to the full length of MTDs in *C. elegans*.

As MAPH-9 is predicted to bind directly to microtubules, we verified that it localizes to the axoneme using super-resolution microscopy. In longitudinal optical sections of the axoneme, GFP::MAPH-9 localized in two discrete bands in a region slightly wider than TBB-4 (Figure 1E and 1F). Additionally, fluorescence recovery after photobleaching experiments revealed that MAPH-9 displayed stable localization to the axoneme, dynamics that were more like the endogenous cilia-specific tubulin isotype TBA-5/α-tubulin than the cilia motor protein OSM-3 (Figure S1E). These data indicate that MAPH-9 is a stable component of MTDs and suggest that MAPH-9 localizes to the outside surface of the axoneme.

MAPH-9 localizes to the centrioles concomitant with the appearance of microtubule doublets

To further test if MAPH-9 specifically recognizes MTDs, we took advantage of a unique aspect of *C. elegans* ciliogenesis. Cilia are built from microtubule-based structures called centrioles that template the assembly of MTDs in the axoneme. *C. elegans* centrioles are normally composed of nine microtubule singlets, but centrioles in ciliated cells build MTDs *de novo* just prior to ciliogenesis (Figure 1G)[31]. We therefore determined if MAPH-9 localizes to the centriole concomitant with the appearance of MTDs, which occurs in the amphid neurons at “bean” stage of embryogenesis (~360mpf, Figure 1H and S1F). Each ciliated neuron has one nuclear-associated centriole and another that migrates to the tip of the dendrite to build the axoneme[32]. GFP::MAPH-9 localized to both centrioles as indicated

by colocalization with the centrosome component SPD-5 beginning at bean stage (Figure 1H). While MAPH-9 that colocalized with the nuclear-associated SPD-5 punctum stayed low, the other dendrite associated MAPH-9 punctum intensified throughout embryogenesis (Figure S1F and S1G), consistent with MAPH-9 recognizing MTDs. We then tracked MAPH-9 localization throughout ciliogenesis in live embryos and observed that MAPH-9 colocalized with TBB-4 in the growing axoneme (Figure 1J, S1H and S1I). Together these data indicate that MAPH-9 localizes to MTDs as they are being built and suggests a role for MAPH-9 in building or maintaining this unique microtubule-based structure.

MAPH-9 preferentially binds polyglutamylated microtubules

Given the ability of MAPH-9 to distinguish between doublet and singlet microtubules *in vivo*, we sought features of the MTD that could impart this specificity. MAP binding to microtubules is influenced by posttranslational modifications (PTMs) of tubulin[33–35], many of which occur in the axoneme[36]. In particular, *C. elegans* cilia are highly polyglutamylated[37]. To determine if the polyglutamylation state of microtubules impacts MAPH-9 binding, we tested the ability of purified recombinant MAPH-9 protein to bind *in vitro* to microtubules with and without polyglutamylation. Tubulin with different levels and patterns of PTMs was purified from the brains of mice mutant for different tubulin-modifying enzymes: 1) mutants for the polyglutamylases TTLL1 and/or TTLL7, which lack polyglutamylation on α- and/or β-tubulin; and 2) mutants for the acetyltransferase αTAT1, which lack tubulin acetylation. Compared to microtubules built from fully posttranslationally modified tubulin from wild-type mice or tubulin lacking acetylation, MAPH-9 showed a significantly reduced binding to microtubules lacking polyglutamylation (Figure 1K, 1L and S1J).

The observation that the lack of both TTLL1-catalyzed α-tubulin polyglutamylation and TTLL7-catalyzed β-tubulin polyglutamylation affected MAPH-9 binding, and that loss of both had an additive effect, suggested that polyglutamylation has a general, and not an enzyme-specific effect on MAPH-9-microtubule interactions. Polyglutamylated tubulin has been previously reported in *C. elegans* to be restricted to a proximal portion of the axoneme that is of similar length to MTDs[30,37]. We confirmed that polyglutamylation is proximally restricted within phasmid axonemes but found this localization to be longer than reported[30] and thus also longer than MAPH-9 localization (Figure S1K and S1L). We next assessed MAPH-9 localization in worms lacking all known glutamylases, *ttll-4, ttll-5*, *ttll-9, ttll-11, tll-15* quintuple mutants (5xE mutant), that have significantly reduced glutamylation (Figure 1N). MAPH-9 localization was significantly shorter in 5xE mutants compared to Control worms (Figure S1M). In addition to this decrease in MAPH-9 length in 5xE mutants, MAPH-9 localization was also reduced per unit length (Figure 1M and 1O). Although we cannot rule out that these effects on MAPH-9 localization are due to axonemal structural defects caused by loss of polyglutamylation,[38] these data indicate a role for polyglutamylation in MAPH-9 localization *in vivo* and *in vitro*.

MAPH-9 modulates motor activity and controls cilia function

To determine whether MAPH-9 plays functional roles within the axoneme, we generated a *maph-9* deletion mutant by replacing the entire coding region with BFP (*maph-9(0),*

Figure 2A). *maph-9(0)* mutants had full length cilia and no defects in taking up external dye through their exposed cilia (Figure 2B and S2A-S2C). We next explored whether MAPH-9 modulates the ability of molecular motors to bind to and walk on microtubules, known roles for MAPs in general[15,33,39]. Indeed, human MAP9 can modulate the binding and/or activity of cytoplasmic microtubule motors *in vitro*[40], but roles with respect to IFT motors found in cilia had not been tested. *C. elegans* cilia use two semi-redundant kinesin-2 anterograde motors (Figure 2C); the heterotrimeric kinesin-II, composed of KLP-11, KLP-20 and KAP-1, and homodimeric OSM-3; with both motors walking on MTDs and only OSM-3 walking on the singlet microtubules in the distal axoneme (Figure 2D)[41]. OSM-3 is sufficient to build a full length axoneme in the absence of kinesin-II, but loss of both kinesin-II and OSM-3 completely abrogates ciliogenesis[42]. To understand if MAPH-9 works in concert with these motors to build or maintain cilia, we measured axoneme length in mutants lacking anterograde motor activity and/or MAPH-9. Loss of *maph-9* in an *osm-3* null mutant background (*osm-3(0)*) did not further impact cilia length compared to *osm-3(0)* mutants alone, indicating that kinesin-II still functions in the absence of MAPH-9 (Figure 2B and S2D). In contrast, double mutants lacking both *maph-9* and the essential kinesin-II component *kap-1* (*maph-9(0)*; *kap-1(0)*) showed a significant decrease in axoneme length compared to *kap-1(0)* mutants alone (Figure 2B and S2D). These results suggest that MAPH-9 affects the function of OSM-3 more than that of kinesin-II.

We directly observed motor activity in *maph-9(0)* mutants, measuring the velocity of motor particles by generating kymographs of endogenously tagged OSM-3 and KAP-1 in Control and *maph-9(0)* mutant axonemes (Figure 2D). KAP-1 movement was significantly faster and OSM-3 was significantly slower in *maph-9(0)* mutants compared to Control (Figure 2E). Since OSM-3 and Kinesin II work together in the proximal axoneme, we isolated the effect of MAPH-9 on individual anterograde motor types by examining each motor in the mutant background of the other. In *kap-1(0)* mutants, OSM-3 moved at the same speed in axonemes with and without MAPH-9 (Figure 2E). In contrast, KAP-1 velocity increased in *osm-3(0); maph-9(0)* double mutants, similar to the effect on KAP-1 in *maph-9(0)* mutants when OSM-3 was present. In addition to changes in velocity, we found a lower frequency of OSM-3 anterograde tracks and a higher frequency of KAP-1 anterograde tracks in *maph-9(0)* mutants compared to Control (Figure 2F). Loss of either motor in combination with *maph-9* led to reduced frequency of the remaining motor (Figure 2F). The velocity of the dynein component XBX-1 was increased in *maph-9(0)* mutants (Figure 2E) and had no change in the frequency of retrograde tracks (Figure 2F). Together, these results indicate that MAPH-9 decreases kinesin-II and dynein velocity, but facilitates OSM-3 function perhaps by regulating its processivity.

Cilia in *C. elegans* sensory neurons mediate diverse behaviors and interactions with the extracellular environment, for example the ability of male worms to locate and copulate with hermaphrodites[43–45], or the emission of non-tactile mate-finding cues by hermaphrodites[46]. To understand if MAPH-9 is required for cilia function, we assessed the mating ability of *maph-9(0)* mutants. MAPH-9 localizes to all cilia of the male tail, but as in other sensory neurons, MAPH-9 was not required for ciliogenesis in these neurons (Figure 2G and S2E). Despite the presence of cilia and no change in brood size (Figure S2F), mating efficiency was significantly reduced when we mated either male or hermaphrodite

maph-9(0) mutants with the greatest observable reduction in mating efficiency when *maph-9(0)* mutant hermaphrodite and males were mated (Figure 2H). These data indicate that although MAPH-9 is not strictly required for ciliogenesis, MAPH-9 mediates cilia function.

Loss of MAPH-9 causes ultrastructural microtubule doublet defects in the axoneme

Given the effect of MAPH-9 on motors and cilia function, we sought to determine whether MAPH-9 plays a structural role at MTDs. Amphid[47] and phasmid cilia (Figure S3A and Movie S1) share similar ultrastructural features, with axonemes originating at the base as 9 MTDs that progress to incomplete doublets and then microtubule singlets at the distal tip. EM analyses of amphid and phasmid cilia in *maph-9(0)* mutants did not indicate any gross morphology defects as cilia were still present (Figure 3A and S3B-S3D) and instead revealed variable structural defects that were specific to MTDs. Overall, *maph-9(0)* mutant amphid cilia had fewer axonemal microtubules compared to wild-type, a defect that became more pronounced towards the distal tip (Figure S3F) and that was marked by an increase of singlet microtubules and fewer incomplete doublets and MTDs in the middle segment (Figure S3G). These defects were most pronounced in the axonemes of the ADL and ASI neurons. In the ADL axoneme which is composed of a high percentage of incomplete doublets in wild-type, *maph-9(0)* mutant axonemes were mainly singlet microtubules in the middle segment (Figure 3A–3C), while in the ASI axoneme we observed a more general loss of microtubules throughout the middle and distal segment in *maph-9(0)* mutants (Figure S3E).

In addition to these more general effects on axonemal architecture, we also found *maph-9(0)* mutant cilia lacked the stereotypical roundness of the B-tubule normally found in wild-type MTDs (Figure 3D and 3E). This effect was specific to the B-tubule as the A-tubule was similarly round in wild-type and *maph-9(0)* mutant axonemes. To further analyze MTD structure, we determined whether *maph-9(0)* mutants contained the normal 13 protofilament A-tubule and 10 protofilament B-tubule as in wild-type. While the A-tubule appeared unaffected, we found that the B-tubule protofilament number was significantly decreased in *maph-9(0)* mutant phasmid cilia, with axonemes frequently containing 8 or 9 protofilaments (Figure 3F and 3G). These ultrastructural defects in *maph-9(0)* mutants suggest that MAPH-9 promotes the assembly and/or stability of MTDs through a more specific role at the B-tubule.

MAPH-9 localization is conserved in mammalian cells

Given the clear role of MAPH-9 in *C. elegans* cilia, we explored whether this function is conserved. MAP9 homologs are conserved in a large subset of metazoans, including in mice, humans, nematodes, and cnidarians, but are absent in nearly all arthropods and tunicates. Although the MAP9 amino acid conservation is poor among metazoans, AlphaFold predictions of MAP9[48,49] across species all contain a single ~202 amino acid long alpha helix (Figure 4A, 4B, S4A, S4B and Table S1), which corresponds to the human MAP9 microtubule binding domain[20] and may represent a coiled coil. We validated a MAP9 antibody (Figure S4C-S4G) to explore MAP9 localization in mammalian cells and tissues. Consistent with previous reports in U-2 OS cells[16,20], MAP9 localized to the mitotic

spindle in hTERT RPE-1 cells (Figure S4H). In addition, MAP9 clearly localized to cilia in interphase hTERT RPE-1 and MDCK-II cells, colocalizing with polyglutamylated tubulin (Figure 4C-4F). Intriguingly, MAP9 localization in cilia was enriched in the proximal region adjacent to the centrosome and diminished toward the distal end of the axoneme (Figure 4C-4F). This MAP9 localization pattern in MDCK-II cells is consistent with the portion of the axoneme that contains MTDs (Figure 4F)[50]. Notably, we observed that MAP9 localization was also restricted to more proximal regions of cilia in mouse tissues, areas known to contain MTDs[51–53]. Specifically, MAP9 localized proximally in the primary cilia of the collecting duct cells in the kidney, motile cilia in the nasal epithelium, the connecting cilium in the photoreceptors of the eye, and along the length of almost the entire flagellar axoneme in developing and mature mouse sperm (Figure 4G, S4I and S4J). Together, these results indicate that MAP9 localizes to the axoneme of mammalian cilia, likely to MTDs, and suggest that polyglutamylation may play a conserved role in refining this localization pattern.

Discussion:

Through endogenous labeling studies of MAPH-9 in *C. elegans*, we identified a role for MAPH-9 and the mammalian homologue MAP9 in cilia. In *C. elegans,* we found a remarkable preference of MAPH-9 for MTDs *in vivo* with MAPH-9 only localizing to MTDs despite its ability to bind singlet microtubules *in vitro*. This preference seems to in part be regulated by polyglutamylation, a post-translational modification that in *C. elegans* is restricted to axonemal microtubules. In mammalian cells and tissues, MAP9 similarly localizes to a more proximal, polyglutamylated portion of the axoneme, but also to spindle microtubules and within neuronal processes, microtubule populations that are decorated with post-translational modifications[34,54,55]. Thus, a unifying feature to localize MAPH-9/MAP9 across these contexts might be polyglutamylation, although certainly in combination with other factors as we found that MAPH-9 bound to microtubules lacking polyglutamylation both *in vitro* and *in vivo*.

Polyglutamylation occurs on the C-terminal tails of α- and β-tubulin[56] and was recently shown to occur specifically on protofilament 9 of the B-tubule in diverse axonemes[57]. Given that the steric suppression of the C-terminal tails is proposed to stimulate B-tubule formation[1], we speculate that MAPH-9 might interact with the C-terminal tails through their polyglutamylation, perhaps helping to reduce their steric hinderance to reinforce the B-tubule. MAPH-9 might also recognize and/or play a role in the non-tubulin-based inner junction between the A and B-tubule[5,58,59]. Since the predominant phenotype in *maph-9* mutants was not the complete loss of MTDs, but rather a malformation of the B-tubule, these roles would be in combination with other factors. Indeed, the loss of MTDs that we observed in a subset of *maph-9* mutant neurons was reminiscent of phenotypes associated with the loss of NPHP-2/Inversin and/or ARL-13[30,60], suggesting that these components work in combination.

MAPs have been proposed in many contexts to influence motor walking on cytoplasmic microtubules[40,61–64] and we found that loss of *maph-9* impacted the movement of all IFT motors. These effects could be due to ultrastructural defects in *maph-9*(0) mutants, however,

we favor a model where IFT motors are directly regulated by MAPH-9 given the specific effect we saw on OSM-3 function in *maph-9(0)* mutants. Interestingly, MAP9 and dual anterograde motor systems are both metazoan innovations found in many phyla (Table S1), and thus perhaps MAP9 modulates these motors to allow for fine tuning of IFT speed and processivity[65].

Finally, MAP9 has been proposed as a target for cancer treatment given its localization to the mitotic spindle[66–68]; however, we have shown that MAP9/MAPH-9 plays an important role in cilia in supporting MTDs and modulating motors. Further investigation into the structure and function of MAP9/MAPH-9 will advance our understanding of the fundamental mechanism of MTD formation, as well as provide insight into how MTDs are dysregulated in ciliopathies.

Limitations of the study

Endogenous tags used for imaging caused no observable phenotypes, however tags may alter protein dynamics and/or function. While MAP9 and MAPH-9 have similar axonemal localization, it is unknown whether they play similar functional roles.

STAR Methods:

RESOURCE AVAILABILITY

Lead Contact—Further information and requests for resources and reagents should be directed to and will be fulfilled by the lead contact, Dr. Jessica L. Feldman (feldmanj@stanford.edu).

Materials Availability—DNA constructs and transgenic *C. elegans* strains generated in this study are available from the Lead Contact, Dr. Jessica Feldman, upon request.

Data and code availability

- All data reported in this paper will be shared by the lead contact upon request.
- Any additional information required to reanalyze the data reported in this paper is available from the lead contact upon request.

EXPERIMENTAL MODEL AND STUDY PARTICIPANT DETAILS

Housing condition and maintenance of experimental animals—*C. elegans* strains were cultured at 20°C on plates of Nematode Growth Medium (NGM) covered with a lawn of OP50 *E. coli*[73]. Strains used in this study are listed in the Key Resources Table.

Wild-type male and female mouse kidneys and P6 nasal epithelium were a gift from the Luo lab at Stanford University. All procedures followed animal care and biosafety guidelines approved by Stanford University's Administrative Panel on Laboratory Animal Care (APLAC 14007) in accordance with NIH guidelines. Wild-type mouse sperm were obtained from male mice and eyes were obtained from male and female mice that were bred at Stanford University (Stanford, CA) or purchased from Jackson Laboratory (JAX) in accordance with the National Institutes of Health and U.S. Department of Agriculture

criteria, and protocols for their care and use were approved by the Institutional Animal Care and Use Committees (IACUC) of Stanford and JAX. Mice were group housed on a 12 hour light/dark cycle with access to food and water ad libitum.

hTERT RPE-1 (human telomerase reverse transcriptase immortalized retinal pigment epithelial cells) were obtained from the American Type Culture Collection (ATTCC) (CRL-4000). hTERT RPE-1 cells were authenticated using STR profiling using CODIS loci. hTERT RPE-1 cells were cultured at 37 °C in 5% CO_2 in Dulbecco's Modified Eagle Medium (DMEM) F12 (1:1) (Gibco) supplemented with 10% Cosmic Calf Serum (HyClone). MDCK-II (Madin-Darby canine kidney) cells were a gift from the Nelson lab. MDCK-II cells were cultured at 37°C in 5% CO_2 in DMEM 4.5g/L glucose, L-glut, sodium pyruvate supplemented with 10% Cosmic Calf Serum (HyClone). MDCK-II and hTERT RPE-1 cells were cultured on 10cm polystyrene tissue culture dishes (Falcon 353003). Cells were passaged with Trypsin 0.25% (Corning).

Husbandry conditions of experimental animals—For all experiments, *C. elegans* embryos and larvae were obtained from hermaphrodites. Embryos were either harvested from the uterus of young, gravid adult hermaphrodites that were incubated in liquid or were picked directly from culture plates after they were laid by hermaphrodites. For strain generation that required genotypic mixing, 5 male and 3 hermaphrodite animals were crossed on 3.5 cm NGM plates seeded with OP50 and cross-progeny were isolated. The desired genotypes were identified either through direct visualization of markers when possible or by PCR genotyping.

METHOD DETAILS

CRISPR/Cas9 cloning and editing—Genes were endogenously edited to create mutants or endogenously tagged proteins using the CRISPR Self Excising Cassette (SEC) method [70]. Cas9 and appropriate sgRNAs were delivered using a plasmid based on pDD162, with the sgRNA (Key Resources Table) incorporated using the Q5 Site directed mutagenesis kit (New England BioLabs). Repair templates for each edit were generated by adding two homology arms flanking the appropriate SEC. Homology arms were generated by amplifying the region close to the desired insertion site (Key Resources Table). The repair vector was digested and homology arms were assembled using a HiFi DNA assembly reaction (New England BioLabs) accordingly to the manufacturer's recommendation. DNA mixtures (sgRNA and Cas9 containing plasmid and repair template) were injected into the germline of adults worms, and CRISPR edited worms were selected by treatment with hygromycin followed by screening for appropriate expression and localization. CRISPR edited worm lines were then backcrossed two times and homozygosed.

RNAi—RNAi treatment was performed by feeding L4 worms with HT115 bacteria transformed with *glo-3* (RNAi) plasmid Bacteria were spread onto NGM plates supplemented with 1mM IPTG and 50 μg/mL Ampicillin and grown for 48 hours at room temperature away from light. L4 stage worms were left on RNAi plates at 25°C for 48 to 72 hours and their progeny were imaged.

Mating efficiency assay—Three L4 hermaphrodites and three L4 males were placed on a 35mm NGM plate spread with OP50 *E. coli* and allowed to mate for 24 hours at 20°C. Male strains included *him-5(e1490)* to generate males and a nuclear intestinal GFP transgene to label cross-progeny. The males and hermaphrodites were then transferred to a fresh plate, allowed to mate for an additional 48 hours, and removed. All cross- and self-progeny were counted on a fluorescent dissecting scope with nuclear intestinal GFP from the males marking cross-progeny and the absence of GFP marking hermaphrodite self-progeny. Each cross was performed in triplicate for each hermaphrodite/male genotype pair.

Brood size—Brood sizes for individual worms over the course of three days were determined for wild-type (PD1074) and *maph-9(0)* (JLF625) worms as follows: Single L4 hermaphrodites were left on freshly seeded plates for 24 hours. They were transferred to a second plate for the next 24 hours, and then to a third plate for another 24 hours and then removed. Hatched larvae for each plate were counted and removed 1–2 days after the mother had been removed. All incubations were at 20°C.

Transfection—Cells were transfected with lipofectamine 3000 reagents (Invitrogen) according to the manufacturer's directions.

Mouse Tissue Handling—Wild-type adult mouse kidneys and eyes were dissected and fixed for 2 hours in 4% PFA in PBS rotating at 4°C. Tissue was washed two times in PBS and equilibrated in a graded series of sucrose solutions (10% and 20%). Tissue was flash frozen in O.C.T compound (Fisher Scientific) in a dry ice/95% ethanol slurry, and kidneys (coronal) and adult mouse eyes (transverse) were cryosectioned at 20 μm. Cauda epididymal sperm were collected after extrusion from the epididymis in PBS. Developing spermatids were assessed via tubule squash preparations from mouse testes.

Immunohistochemistry

MDCK-II cells: Cells were seeded to confluency on 12 mm coverslips in 24 well plates. Cells were grown for 7 days and fixed without starvation. Mature ciliation timepoints were grown for 21 days and then starved in 0.5% serum DMEM media for 48 hours before fixation as has been previously reported[50]. Cells were fixed in 4% PFA in PBS for 15 min at room temperature. Coverslips were blocked for 1 hour at room temperature in PBS-BT (3% BSA, 0.1% Triton-X-100 in PBS) before incubating with primary antibodies in PBS-BT overnight at 4°C. Coverslips were washed 3× 5min in PBS-BT then stained with secondary antibodies 1:1000 in PBS-BT for 45 min – 1hr at room temperature. Cells were washed 3 times for 5 minutes before mounting in vectashield + DAPI (1:10,000) (Vector Laboratories H-2000) and sealed with nail polish. Antibodies indicated in the key resources table were used at the following concentration: mouse IgG2b anti-acetylated tubulin 6–11B-1 (1:1000), rabbit anti-MAP9 (1:100), mouse IgG1 anti-polyglutamylated tubulin GT335 (1:500), Goat anti-mouse IgG2b 488 (1:1000), Goat anti-rabbit 568 (1:1000), Goat anti-mouse IgG1 647 (1:1000).

hTERT RPE-1 cells: Cells were seeded to confluency on 12 mm coverslips in 24 well plates and grown for 5 days without starvation. Cells were fixed and mounted as indicated

for MDCK-II cells. Antibodies indicated in the key resources table were used at the following concentration: mouse IgG2b anti-acetylated tubulin 6–11B-1 (1:1000), rabbit anti-MAP9 (1:100), mouse IgG2a anti-centrin 20H5 (1:200), goat anti-mouse IgG2b 568 (1:1000), goat anti-rabbit 488 (1:1000), goat anti-mouse IgG2a 647, DAPI (1:10,000).

Mouse kidneys, eyes, and nasal epithelium: Frozen sections were dried at room temperature, washed once in PBS (5 min. at room temperature), once in PBT (1% Triton X-100 in PBS), and blocked (10% goat serum + 1% BSA in PBT) for 1 hour at room temperature. Samples were incubated with primary antibodies overnight at 4°C, washed 2 times in PBT, incubated in species-specific secondary antibodies at room temperature for 1 hour, and then incubated for 5 minutes with DAPI (4',6-diamidino-2-phenylindole, Thermo Fisher Scientific) (0.5μg/mL in PBS). Antibodies indicated in the key resources table were used at the following concentration for kidney and eyes: rabbit anti-MAP9 (1:100), mouse IgG2b anti-acetylated tubulin 6–11B-1 (1:1000), Goat anti rabbit-488 (1:1000), goat anti-mouse IgG2b 568 (1:1000), DAPI (1:10000). For nasal epithelium: rabbit anti-MAP9 (1:100), mouse IgG2b anti-acetylated tubulin 6–11B-1 (1:1000), Goat anti rabbit-568 (1:1000), goat anti-mouse IgG2b 488 (1:1000), DAPI (1:10,000).

Mouse sperm: Epididymal sperm were attached to microscope slides for 30 minutes and fixed with 4% PFA in PBS for 15 minutes. The slides were washed with PBS three times before permeabilizing with −20°C methanol for 2 minutes. Slides were washed with PBS three times and incubated overnight at 4°C in antibody dilution buffer (ADB; 3% bovine serum albumin (BSA), 10% horse serum, 0.05% Triton X-100) containing primary antibodies. Slides were washed three times in PBS before applying secondary antibodies diluted in ADB and incubated overnight at 4°C. Secondary antibodies conjugated to Alexa 488, 568, or 633 against rabbit and mouse IgG (Thermo Fisher Scientific) were used at 1:500 dilution. Epididymal sperm immunofluorescence slides were mounted in Mowiol® 4–88 (EMD Millipore) mounting medium containing DAPI (Thermo Fisher Scientific). Antibodies indicated in the key resources table were used at the following concentration for spermatazoon: rabbit anti-MAP9 (1:100), mouse IgG2b anti-acetylated tubulin 6–11B-1 (1:1000), Goat anti rabbit-488 (1:1000), goat anti-mouse IgG2b 568 (1:1000), DAPI (1:10,000). For elongating spermatid: rabbit anti-MAP9 (1:100), mouse IgG1 anti-alpha-tubulin (1:1000), Goat anti-rabbit 488 (1:1000), goat anti-mouse IgG1 568 (1:1000), DAPI (1:10,000).

C. elegans: Staged young adults were cut in 1x M9 solution and attached to microscope slides coated with poly-lysine and containing Teflon spacers. Slides were frozen on dry ice, animals were permeabilized by freeze-crack method and submerged in 100% MeOH for 5–10 minutes at −20°C. Slides were submerged for 5 minutes twice in PBS, then once in PBT (PBS plus 0.1% Tween). Slides were incubated in primary antibody overnight at 4°C. Slides were then washed in PBT for 5 minutes three times and then incubated in secondary antibody overnight at 4°C. Slides were washed once in PBT then twice in PBS, mounted in Vectashield (Vector Laboratories), and stored at 4°C. Antibodies indicated in the key resources table were used at the following concentration: anti-GFP mouse IgG2A (1:500),

mouse IgG1 anti-polyglutamylated tubulin GT335 (1:500), goat anti-mouse IgG2A 568, goat anti-mouse IgG1 488 (1:1000), DAPI (1:10,000).

Biochemistry

Protein Purification: Protein expression plasmids were transformed into BL21 DE3 cells (Sigma-Aldrich). Starter cultures were inoculated with one colony and grown overnight in 5mL of LB at 37°C supplemented with kanamycin. The starter culture was added to 500 mL of LB with kanamycin, grown at 37°C until OD600 was 0.6, then grown at 18°C for 30 minutes and induced with a final concentration of 100 μM IPTG. Bacteria were pelleted and resuspended in lysis buffer (250 mM NaH_2PO_4, pH 8.0, 2.5 M NaCl, Halt Protease Inhibitor Cocktail (Thermo Fisher Scientific)), lysed using Cell Disruptor MC (Constant System), and centrifuged at 3000 x g for 10 minutes. The supernatant was added to nickel resin Ni-NTA Agarose (Invitrogen) equilibrated in lysis buffer and incubated on a nutator for 1 hour at 4°C. The agarose was centrifuged at 800 x g for one minute and washed with wash buffer (250 mM NaH_2PO_4, pH 8.0, 2.5 M NaCl, 20 mM imidazole, pH 6.0) 3 times. Protein was eluted with elution buffer (250 mM NaH_2PO_4, pH 8.0, 2.5 M NaCl, 250 mM imidazole, pH 6.0).

Antibody Pre-absorption: Proteins were resolved by SDS-PAGE and transferred to nitrocellulose membrane. The membrane was stained with Ponceau S solution (Sigma-Aldrich) for 15 minutes and rinsed twice with water. The membrane around the bands corresponding to GFP and GFP::MAP9 was excised. The membranes were blocked with 5% milk in TBST buffer (Tris- buffered saline with 0.1% Tween-20) for 1 hour at room temperature rinsed twice in TBST buffer, and twice in PBS-BT buffer (3% BSA, 0.1% Triton X-100 in PBS), and then incubated with primary antibody mixture with MAP9, and acetylated tubulin antibodies on a nutator for 5 hours at room temperature. The membranes were then discarded and the antibody mixture was added onto coverslips to stain them for immunofluorescence as described above.

Western Blotting: Samples were denatured with 6X sodium dodecyl sulfate (SDS) Laemmli buffer and boiled at 95°C for 10 minutes. Proteins were separated by SDS-PAGE and transferred to a nitrocellulose membrane (Bio-Rad). The membrane was blocked with nonfat milk at room temperature for 1 hour and then incubated with primary antibodies at 4°C overnight. The membrane was incubated with secondary antibodies at room temperature for 1 hour. All blots were imaged with an Azure 600 (Azure Biosystems) and analyzed using imageJ.

In vitro Microtubule Polymerization: Mouse wild-type tubulin as well as mouse tubulin with post-translation modification (*Ttll1*$^{-/-}$, *Ttll7*$^{-/-}$, *Ttll1*$^{-/-}$*Ttll7*$^{-/-}$, *Atat1*$^{-/-}$) was purified as previously described[35] . *GMPCPP-lattice microtubules* (*GMPCPP* polymerized) with post-translation modification were polymerized from 4 mg/ml mouse tubulin (wild-type, *Ttll1*$^{-/-}$, *Ttll7*$^{-/-}$, *Ttll1*$^{-/-}$*Ttll7*$^{-/-}$, *Atat1*$^{-/-}$) for 1 h at 37°C in BRB80 (80 mM PIPES, 1 mM MgCl2, 1 mM EGTA, pH 6.8 with KOH) (supplemented with 2.7 mM *GMPCPP* (Jena Bioscience). The polymerized microtubules were centrifuged for 30 minutes at 18000

x g in a Microfuge 18 Centrifuge (Beckman Coulter). After centrifugation the pellet was resuspended in BRB80.

In vitro Binding to Microtubule Lattice With Different Post-Translation Modification: Mouse *GMPCPP*-wild-type microtubules were immobilized on anti-tubulin antibody treated channels [74]. Then the channels were flushed with 40 µL of BRB80 to remove unbound microtubules and a snapshot was taken to mark the position of wild-type microtubules. Subsequently *GMPCPP*-mouse microtubules with post-translation modification (*Ttll1*$^{-/-}$, *Ttll7*$^{-/-}$, *Ttll1*$^{-/-}$*Ttll7*$^{-/-}$, *Atat1*$^{-/-}$) were immobilized and the channels were flushed with 40 µl of BRB80 to remove unbound microtubules and again a snapshot was taken to mark the position of microtubules with post-translation modification. Finally, the flow chamber was flushed with 10 µl of 20 nM GFP-MAPH9 diluted in the assay buffer (BRB80, 0.2% Tween20, 0.5 mg/ml Casein, 20 mM D-glucose, 0.22 mg/ml glucose oxidase and 20 mg/ml catalase). Time-lapse image sequences of MAPH9 binding to microtubules were recorded for 1 min at the rate of 1 frame per second with an exposure time of 100 ms. Data from three independent experiments was collected, each experiment was repeated on at least three days.

Microscopy

***C. elegans* Worm Imaging:** Worms were mounted on an agarose pad (5% agarose dissolved in M9) immersed in 1mM levamisole (Sigma-Aldrich) sandwiched between a microscope slide and no. 1.5 coverslip. Embryos were mounted on an agarose pad (3% agarose dissolved inM9) without levamisole.

Late-Stage *C. elegans* Embryo Imaging: Embryos at the 1.5-fold stage were selected by manual picking and then excised from the NGM plate to a humidified chamber to be aged. At the designated time after the 1.5-fold stage, embryos were placed in an airtight chamber with an intake valve for CO_2 delivery from dry ice and an exhaust valve. After incubation with CO_2 for 15 minutes, the chamber was sealed and imaged as described below.

Dye Filling Assay: Young adult worms were incubated in 5 µg/ml DiI (1,1′-dioctadecyl-3,3,3′, 3′-tetramethylindocarbocyanine perchlorate, Medchemexpress) diluted in M9 for 1hour. Worms were then washed 3 times in M9 and placed onto NGM plates for 2 hours for destaining. Dye filled worms were mounted and imaged as above.

Spinning-disk Confocal Microscopy: Unless indicated, all images were acquired using a Nikon Ti-E inverted microscope (Nikon Instruments), a Yokogawa CSU-X1 confocal spinning disk head, and an Andor Ixon Ultra back thinned EM-CCD camera (Oxford Instruments - Andor), controlled by NIS Elements (Nikon Instruments). Images were obtained using a 60x (NA= 1.4) or 100x Oil Plan Apochromat objective (NA= 1.45). Z stacks were acquired using a 0.2 µm step. For timelapse of motor movement, images were acquired at 150 ms exposure with no delay for 1 minute.

Confocal microscopy images of MDCK-II cells were acquired as z-stacks with a 0.4 µm step size using a Zeiss Axio Observer Microscope (Carl Zeiss) with a PlanApoChromat 63x/1.4NA objective and 1.6x optivar, Prime BSI Express sCMOS camera (Photometrics),

and CSU-W1 spinning disk (Yokogawa). The microscope was controlled using Slidebook software (Intelligent Imaging Innovations). Images were acquired with no gain and 100 ms exposure per channel with 100% laser power.

Widefield Microscopy: Widefield images were acquired using a Nikon Eclipse Ni upright microscope (Nikon Instruments), Lumencore Sola Light Engine, and a Andor Zyla DG-152V-C1E-F1 5.5 Megapixel Front illuminated Scientific CMOS (Oxford Instruments – Andor), controlled by NIS Elements (Nikon Instruments). Images were obtained using a 40x (NA=1.30) oil or 60x (NA=1.4) oil. Z stacks were acquired using a 0.3 μm step.

TIRF microscopy: Total internal reflection fluorescence (TIRF) microscopy experiments were performed on an inverted microscope (Nikon-Ti E, Nikon-Ti2 E) equipped with 60x or 100x NA 1.49 oil immersion objectives (Apo TIRF or SR Apo TIRF, respectively, Nikon Instruments) and either Orca Flash 4.0 sCMOS (Hamamatsu) or PRIME BSI (Teledyne Photometrics) cameras. An additional 1.5x magnifying tube lens was used. Microtubules were visualized by using an epifluorescence lamp and GFP-MAPH9 with HiLyte-647 tubulin [74]were visualized sequentially by switching between microscope filter cubes for Cy5 and GFP channels. The imaging setup was controlled by NIS Elements software (Nikon Instruments). Flow chambers for TIRF imaging assays were prepared as described previously [75]. Channels were treated with anti-biotin antibody solution (Sigma-Aldrich, 1 mg/ml in PBS) or alternatively with anti-tubulin antibody (Sigma-Aldrich, 1 mg/ml in PBS) solution after 5 minutes, followed by one-hour incubation with 1% Pluronic F127 (Sigma-Aldrich).

Structured illumination microscopy (SIM): Structured illumination microscopy images were acquired on an OMX BLAZE V4 microscope (GE healthcare) in the Stanford Cell Science Imaging Facility equipped with a U-PLANAPO 100x SIM (NA = 1.4) objective (Nikon Instruments) and Evolve 512 emCCD cameras (Teledyne Photometrics) controlled by DeltaVision software. Structured Illumination images were generated using SoftWoRx (GE healthcare). Pixel size of reconstructed images is 40.35 nm giving us an effective resolution of 100–120 nm in *C. elegans* tissues. Images were adjusted for brightness and contrast using FIJI.

Ultrastructure expansion microscopy (U-ExM): hTERT RPE-1 cells: Cells were grown on 12 mm, no. 1.5 glass coverslips. Coverslips were fixed in methanol at 20°C for 10 minutes and washed with 1x PBS. Coverslips were incubated overnight at 37°C in an acrylamide/formaldehyde solution (AA/FA, 0.7% formaldehyde, 1% acrylamide in PBS). Gelation was allowed to proceed in monomer solution (19% sodium acrylate, 10% acrylamide, 0.1% bis-acrylamide, 0.5% ammonium persulfate-APS, 0.5% TEMED) and the coverslips were discarded. Gels were boiled at 95°C in denaturation buffer (200 mM SDS, 200 mM NaCl, 50 mM Tris pH 9) for 1 hour. Denaturation buffer was removed, gels were washed with multiple water rinses and allowed to expand in water at room temperature overnight. Small circles (approximately 5 mm in diameter of each expanded gel) were excised and incubated with primary antibodies diluted in PBSBT buffer (3% BSA, 0.1%Triton X-100 in PBS) on a nutator at 4°C overnight. The next day, gels were washed

three times with PBSBT buffer and incubated with secondary antibodies and 5 μg/mL DAPI diluted in PBSBT, on a nutator at 4°C overnight. Gels were washed once with 1X PBS and three times with water, and placed in a glass- bottom, poly-L-lysine treated 35mm plate to image.

C. elegans: Worms were grown on NGM plates, collected in tube by washes with M9 and left sitting on ice for 5 minutes to let them sink at the bottom of the tube. Worms were then collected in a 1.5 mL microcentrifuge tube and washed with M9 by centrifuging them 3 minutes at 400 x g (these centrifugation parameters are used through the entire process unless specified) until no bacteria was visible in the supernatant. Worms were then centrifuged and topped with 1 mL of fresh 4% formaldehyde in PBS. Worms were incubated 15 minutes at room temperature followed by 4 hours under agitation at 4°C. Following fixation, worms were washed three times with PBS and the cuticle was reduced by incubating fixed worm overnight at 4°C under agitation in a denaturation solution (5% β-mercaptoethanol, 10 mM DTT, 1% Triton X-100, 120 mM Tris pH 7.0). Worms were then washed 5 times in PBS and incubated 2 hours at 37°C in collagenase solution (1kU/mL Type VII Collagenase, 100 mM Tris pH 7.4, 1mM $CaCl_2$, 0.1% Triton X-100). Worms were washed 3 times in PBS, before being centrifuged in a 12-well plate, 3 minutes at 800 x g, on top of a 12mm round coverslip that had been ethanol cleaned and poly-L-lysine treated. Coverslip were incubated overnight at 37°C in an acrylamide/formaldehyde solution (AA/FA, 0.7% formaldehyde, 1% acrylamide in PBS). Gelation was allowed to proceed in monomer solution (19% sodium acrylate, 10% acrylamide, 0.1% bis-acrylamide, 0.5% ammonium persulfate-APS, 0.5% TEMED) and the coverslips were discarded. Gels were denatured overnight at 37°C in collagenase solution (500U/mL, 100 mM Tris pH 7.4, 1mM $CaCl_2$, 0.1% Triton X-100, 1X PBS). Collagenase buffer was removed, gels were washed with multiple 1X PBS rinses and then boiled at 95°C in denaturation buffer (200 mM SDS, 200 mM NaCl, 50 mM Tris pH 9) for 1 hour. Denaturation buffer was removed, gels were washed with multiple water rinses and allowed to expand in water at room temperature overnight. Small circles (approximately 5 mm in diameter of each expanded gel) were excised and incubated with primary antibodies diluted in PBT+BSA buffer (1% BSA, 0.1%Triton X-100 in PBS) on a nutator at 4°C overnight. The next day, gels were washed three times with PBT buffer and incubated with secondary antibodies diluted in PBT+BSA buffer, on a nutator at 4°C overnight. Gels were washed once with 1X PBS and three times with water, and placed in a glass-bottom, poly-L-lysine treated 35mm plate to image.

Electron microscopy: Age-matched *maph-9(0)* mutants and wild-type worms were prepared for conventional electron microscopy by high-pressure freezing and freeze-substitution. Worms in M9 media supplemented with 20% BSA and OP50 *E. coli* were put in specimen carriers with a 50μm deep well (Technotrade International), covered with the flat side of a type B specimen carrier (Technotrade International), and frozen using a Leica EM ICE high pressure freezer. Freeze-substitution was done with a Leica AFS2 unit in acetone with 1% OsO_4, 0.1% uranyl acetate, 1% methanol and 3% water [76,77]. After substitution, samples were rinsed in acetone, infiltrated, and then polymerized in Eponate 12 resin (Ted Pella). Care was taken during resin embedding to orient the worms for optimal

cross sectioning orientation. Serial 50-nm cross-sections through the amphid and phasmid cilia of worms were cut with a Leica UC7 ultramicrotome using a Diatome diamond knife. Sections were picked up on Pioloform-coated slot grids and stained with uranyl acetate and Sato's lead [78]. Sections were imaged with an FEI Tecnai T12 transmission electron microscope at 120 kV using a Gatan Rio 4k × 4k camera and DigitalMicrograph. During imaging, the axis of the cilium was adjusted as best as possible to match the optical axis of the TEM utilizing a Fischione Model 2040 dual-axis tomography holder (Fischione Instruments, Inc). This was particularly necessary for phasmid cilia which unlike amphid cilia, are oriented at an angle to the anterior-posterior axis of the tail. Serial sectioning for amphid cilia was started at the anterior tip of the worm and continued for 30–40 μm posteriorly; for phasmid cilia sectioning was started at the anal pore and continued posteriorly beyond the exit of the cilium tip through the cuticle. For amphid cilia quantification, images were aligned to the amphid socket auto-junction[47].

Electron Microscopy Reconstruction: Serial section images stacks were converted from TIFF to MRC format using the tif2mrc command in the 3dmod package of IMOD[79]. MRC stacks where then used with the 3dmod package from IMOD to perform the segmentation. Cilia membrane and microtubules were manually traced in IMOD using 3dmod. In cases where the microtubules were not objectively identifiable, above and below stack images were used to estimate the structure, however if this approximation led to unidentifiable structures/densities, no segmentation was performed. Video S1 was generated using the video editor of the 3dmod and annotated using Adobe Photoshop.

Fluorescence Recovery After Photobleaching (FRAP): FRAP experiments were performed on the spinning-disk confocal microscope described above using a 405nm laser for photobleaching and a 60X objective lens to image young adult worm phasmid axonemes. The region of interest (ROI) was selected (middle segment) and photobleached for 1000ms using a Mosaic photostimulation system (Andor). Images were acquired every 5 seconds for a total of 24 frames. Images were stabilized using the Fast4Dreg plugin of Fiji[80,81]. Fluorescence intensity was quantified using Fiji and normalized by 1) dividing the value of the fluorescence of bleached area with the fluorescence of the unbleached distal segment of the axoneme, and 2) dividing each normalized value by the maximum normalized fluorescence intensity of that time point.

Phylogenetics and AlphaFold structural predictions—Homologs to human MAP9 (see Table S1) were identified through: 1) BLAST or PSI-BLAST to NCBI databases using default values 2) proteins containing MAP9 domain IPR026106 that also contained AlphaFold v2 structural predictions[48,49]. Protein sequences of homologs were aligned using Muscle[82] and trimmed to conserved parts (total of 92 positions) within the main alpha helix in JalView[83]. A maximum likelihood tree was constructed using PhyML 3.0[84] with bootstrap support values from 1000 repeats and substitution model chosen by the Akaike Information Criterion[85]. Nodes with support less than 250/1000 are not shown on tree after visualization in FigTree v1.4.4. AlphaFold v2 structural prediction images and the identity of the longest righthanded alpha helix were obtained from the AlphaFold Protein Structure database and associated mmCIF files. Mouse and worm MAP9 homologs were aligned via

pymol super and colored from grey to green/blue by pLDDT (spectrum b, grey lightblue blue, AF-Q3TRR0-F1mod; spectrum b, grey palegreen green, AF-Q18452-F1-mod).

QUANTIFICATION AND STATISTICAL ANALYSES

Image Quantification

Circularity measurement (Electron Microscopy): Measurements were performed using the Fiji on EM images of both left and right phasmid pairs at different positions along the length of the middle segment. Only MTDs where both A and B-tubules were oriented in plane were measured. A- and B-tubules were manually traced with the freehand tool and the roundness value was determined by analyzing the trace for circularity (4π(area/perimeter^2). The number of worms and microtubules assessed were: wild-type: 2 worms, 6 cilia, 113 microtubules considered, 33 microtubules not considered; *maph-9(0)*: 2 worms, 8 cilia, 137 microtubules considered, 104 microtubules not considered.

Protofilament count (Electron Microscopy): EM images of control and *maph-9(0)* phasmids were randomized. Five scorers counted protofilament number in MTDs where both A- and B-tubules were oriented in plane and the B-tubule was complete: wild-type: 8 images, 6 cilia, 2 worms, 33 MTDs counted out of 143 MTDs (23% counted); *maph-9(0)*: 9 images, 8 cilia, 2 worms, 31 MTDs counted out of 148 MTDs (21% counted)). The protofilament number for each MTD was the mode among the scorers (wild-type: 2 worms, 6 cilia; *maph-9(0)*: 2 worms, 8 cilia).

Ciliary Area Measurement (Electron Microscopy): Measurements were performed using Fiji on EM images of both left and right phasmid pairs at different positions along the length of the middle segment. Membranes were manually traced with the freehand tool and the area value was determined from the trace area. The number of worms and sections assessed were: wild-type: 2 worms, 6 cilia, 2 sections; *maph-9(0)*: 2 worms, 8 cilia, 2 sections

Fluorescence Length in Phasmids: Images were imported into Fiji and the 20 z-planes of 0.2 μm spanning an individual pair of phasmids were max projected. The length of each signal was measured using the segmented line tool to trace through the center of the fluorescence. For MAPH-9 or XBX-1 (Fig. 1D, S1H, S1M), the line was traced from the most proximal to the most distal pixel above an estimated 35% of max intensity along the continuous line profile. For TBB-4 and TBA-5 (Fig. 2B, S2B), the line was traced from the center of the base marker/SPD-5 to the most distal pixel above estimated 35% of max intensity along the line profile.

Fluorescence Intensity Measurements in *C. elegans* cilia: Images were imported into Fiji and the 20 z-planes of 0.2 μm spanning the cilium were sum projected. Fluorescence intensity was obtained by tracing the signal using the segmented line tool. A similar line was drawn just outside the axoneme to generate a background measurement. To calculate normalized fluorescence intensity, the average fluorescence along the line profile was subtracted by the average background intensity and the resulting value was divided by the average background intensity. To compare MAPH-9 localization to ARL-13 (Fig. S1D), a 6 μm line was drawn through the MAPH-9 signal beginning at the proximal end of MAPH-9

localization and compared to ARL-13 localization along the same line. Measurements were binned in 0.5 μm intervals along the line. To compare MAPH-9 to polyglutamylated tubulin localization (Fig. S1K), a line was drawn from the most proximal end to the distal end the polyglutamylated tubulin localization and the signal of either protein along this line was compared. Measurements were binned in 10 percent length intervals along the cilium. To calculate normalized fluorescence intensity per length (Fig. 1O) intensity measurements were divided by the measured length as described above.

Fluorescence Intensity Measurements in hTERT RPE-1 Cilia: Images were imported into Fiji and the 20 z-planes of 0.2 μm spanning the cilium were sum projected. Cilium length was obtained using the segmented line tool to trace the signal in both the polyglutamylated tubulin and acetylated tubulin from the distal-most end of the centriole to the distal tip of the axoneme. Background measurements were taken by drawing a similar length line outside of the cilium and averaging the fluorescence for each channel. Reported fluorescence measurements (percent of max intensity) were calculated by subtracting averaged background measurement and dividing this value by the maximum background subtracted value in each line profile. Measurements were binned in 10 percent length intervals along the cilium.

Fluorescence Intensity Measurements in MDCK-II Cilia: Cilia were measured using the Simple Neurite Tracer plugin (v4.1.14) for Fiji[86]. Cilia were traced in 3 dimensions on the acetylated tubulin channel using cursor-autosnapping within 12 XY pixels and 2 z-planes and linescans 1 pixel wide in each fluorescent channel were exported as csv files. Linescans were individually normalized to the minimum and maximum pixel intensity of each cilium then binned into 2 μm wide bins with Python 3.7.6 implemented in Jupyter Notebook 6.4.6.

Motor Tracking: Time lapse images were imported into Fiji and kymographs were generated using the KymographClear2.0 plugin[72]. Tracks were traced manually on each kymograph and imported into KymographDirect software[72] where speeds were calculated automatically. To calculate the number of tracks, in KymographDirect, tracks were adjusted with the same contrast and brightness and counted manually. All motor tracking was performed on proteins that had been endogenously labeled with a fluorescent tag. We acknowledge that endogenous tags have the ability to change the behavior of the protein to which they are attached. Of note, we found that although endogenously tagged KAP-1::GFP has the same velocity as published transgenic KAP-1::GFP[87,88], we observed different speeds between these two proteins in an *maph-9(0)* mutant background (endogenous KAP-1::GFP:[*maph-9(0)*:731.9±206.3 n=478]; KAP-1::GFP transgene:[*maph-9(0); kap-1(0)*: 592.5±157.1 n=225). Since the transgenic KAP-1::GFP must be observed in a *kap-1(0)* background, it is also plausible that this background has synthetic interactions with the *maph-9(0)* mutant background.

In vitro MAPH-9 density estimation: MAPH-9 density on microtubules with different post-translation modifications was measured In Fiji by drawing a rectangle around the microtubule and measuring the average intensity per pixel. The rectangle was then moved to an area directly adjacent to the microtubule where no microtubule is present and the average

intensity per pixel was measured again and subtracted from of the average intensity per pixel for the microtubule. The final density of MAPH-9 was normalized to the average density of MAPH-9 on wild-type microtubules.

Statistical Analysis: Statistical significance tests were performed using Excel with the TTEST function (Student's t-Test). A two-tailed distribution and two-sample unequal variance (heteroscedastic) were assumed. p-value needed for significance was less than 0.05. Statistical tests, samples sizes and sample definitions, and whether standard deviation or standard error were used are all indicated in the figure legends.

Supplementary Material

Refer to Web version on PubMed Central for supplementary material.

Acknowledgements

We thank Erwin Peterman, Guangshou Ou, Liqun Luo, and Kassandra Ori-McKenney for providing *C. elegans* strains, mice, protein, antibody, and advice. We also thank members of the Feldman lab for helpful discussions about the manuscript. This work was supported by: NIH [CMB training grant T32GM007276 (M.V.T. and N.V.M.); K99GM135489 (M.D.S.), K99GM131024 (J.T.W.), F32GM142181 (A.F.L.), R01GM136902 and R01GM133950 (J.L.F.), R01NS082208 (K.S.), R35GM130286 and R01NS082208 (T.S.), R15GM114727 and R15GM135886 (N.P.)]; AHA Postdoctoral Fellowships (S.R.W and J.W.F.); Damon Runyon Cancer Research Foundation Postdoctoral Fellowship DRG-2428-21 (L.E.C.); Howard Hughes Medical Institute (K.S.); Institut Curie, French National Research Agency award ANR-20-CE13-0011, and Fondation pour la Recherche Médicale grant DEQ20170336756 (C.J.); Fondation Vaincre Alzheimer FR-16055p and France Alzheimer grant 2023 (M.M.M.); Institut Curie 3-I PhD Program (IC-3i) and EMBO short-term fellowship 8843 (M.G.); Czech Science Foundation grant 19-27477X and CAS RVO: 86652036 (Z.L.); 1S10OD01227601 from the National Center for Research Resources (NCRR) supported this project, the contents of which do not necessarily represent the official views of the NCRR or the NIH. Some nematode strains were provided by the Caenorhabditis Genetic Center, which is funded by the NIH Office of Research Infrastructure Programs (P40 OD010440).

References

1. Schmidt-Cernohorska M, Zhernov I, Steib E, Le Guennec M, Achek R, Borgers S, Demurtas D, Mouawad L, Lansky Z, Hamel V, and Guichard P. (2019). Flagellar microtubule doublet assembly in vitro reveals a regulatory role of tubulin C-terminal tails. Science 363, 285–288. 10.1126/science.aav2567. [PubMed: 30655442]
2. Nicastro D, Schwartz C, Pierson J, Gaudette R, Porter ME, and McIntosh JR (2006). The molecular architecture of axonemes revealed by cryoelectron tomography. Science 313, 944–948. 10.1126/science.1128618. [PubMed: 16917055]
3. Pigino G, Maheshwari A, Bui KH, Shingyoji C, Kamimura S, and Ishikawa T. (2012). Comparative structural analysis of eukaryotic flagella and cilia from Chlamydomonas, Tetrahymena, and sea urchins. J Struct Biol 178, 199–206. 10.1016/j.jsb.2012.02.012. [PubMed: 22406282]
4. Sui H, and Downing KH (2006). Molecular architecture of axonemal microtubule doublets revealed by cryo-electron tomography. Nature 442, 475–478. 10.1038/nature04816. [PubMed: 16738547]
5. Yanagisawa HA, Mathis G, Oda T, Hirono M, Richey EA, Ishikawa H, Marshall WF, Kikkawa M, and Qin H. (2014). FAP20 is an inner junction protein of doublet microtubules essential for both the planar asymmetrical waveform and stability of flagella in Chlamydomonas. Mol Biol Cell 25, 1472–1483. 10.1091/mbc.E13-08-0464. [PubMed: 24574454]
6. Owa M, Uchihashi T, Yanagisawa HA, Yamano T, Iguchi H, Fukuzawa H, Wakabayashi KI, Ando T, and Kikkawa M. (2019). Inner lumen proteins stabilize doublet microtubules in cilia and flagella. Nat Commun 10, 1143. 10.1038/s41467-01909051-x. [PubMed: 30850601]
7. Ma M, Stoyanova M, Rademacher G, Dutcher SK, Brown A, and Zhang R. (2019). Structure of the Decorated Ciliary Doublet Microtubule. Cell 179, 909–922 e912. 10.1016/j.cell.2019.09.030. [PubMed: 31668805]

8. Dutcher SK, Morrissette NS, Preble AM, Rackley C, and Stanga J. (2002). Epsilon-tubulin is an essential component of the centriole. Molecular biology of the cell 13, 3859–3869. 10.1091/mbc.e02-04-0205. [PubMed: 12429830]

9. Wang JT, Kong D, Hoerner CR, Loncarek J, and Stearns T. (2017). Centriole triplet microtubules are required for stable centriole formation and inheritance in human cells. eLife 6. 10.7554/eLife.29061.

10. Mottier-Pavie V, and Megraw TL (2009). Drosophila bld10 is a centriolar protein that regulates centriole, basal body, and motile cilium assembly. Mol Biol Cell 20, 2605–2614. 10.1091/mbc.E08-11-1115. [PubMed: 19321663]

11. Wei Q, Zhang Y, Schouteden C, Zhang Y, Zhang Q, Dong J, Wonesch V, Ling K, Dammermann A, and Hu J. (2016). The hydrolethalus syndrome protein HYLS-1 regulates formation of the ciliary gate. Nat Commun 7, 12437. 10.1038/ncomms12437. [PubMed: 27534274]

12. Caspary T, Larkins CE, and Anderson KV (2007). The graded response to Sonic Hedgehog depends on cilia architecture. Dev Cell 12, 767–778. 10.1016/j.devcel.2007.03.004. [PubMed: 17488627]

13. Cevik S, Hori Y, Kaplan OI, Kida K, Toivenon T, Foley-Fisher C, Cottell D, Katada T, Kontani K, and Blacque OE (2010). Joubert syndrome Arl13b functions at ciliary membranes and stabilizes protein transport in Caenorhabditis elegans. J Cell Biol 188, 953–969. 10.1083/jcb.200908133. [PubMed: 20231383]

14. Conkar D, and Firat-Karalar EN (2021). Microtubule-associated proteins and emerging links to primary cilium structure, assembly, maintenance, and disassembly. FEBS J 288, 786–798. 10.1111/febs.15473. [PubMed: 32627332]

15. Bodakuntla S, Jijumon AS, Villablanca C, Gonzalez-Billault C, and Janke C. (2019). Microtubule-Associated Proteins: Structuring the Cytoskeleton. Trends Cell Biol 29, 804–819. 10.1016/j.tcb.2019.07.004. [PubMed: 31416684]

16. Saffin JM, Venoux M, Prigent C, Espeut J, Poulat F, Giorgi D, Abrieu A, and Rouquier S. (2005). ASAP, a human microtubule-associated protein required for bipolar spindle assembly and cytokinesis. Proc Natl Acad Sci U S A 102, 11302–11307. 10.1073/pnas.0500964102. [PubMed: 16049101]

17. Forman OP, Hitti RJ, Boursnell M, Miyadera K, Sargan D, and Mellersh C. (2016). Canine genome assembly correction facilitates identification of a MAP9 deletion as a potential age of onset modifier for RPGRIP1-associated canine retinal degeneration. Mamm Genome 27, 237–245. 10.1007/s00335-016-9627-x. [PubMed: 27017229]

18. Fontenille L, Rouquier S, Lutfalla G, and Giorgi D. (2014). Microtubule-associated protein 9 (Map9/Asap) is required for the early steps of zebrafish development. Cell Cycle 13, 1101–1114. 10.4161/cc.27944. [PubMed: 24553125]

19. Liu Q, Tan G, Levenkova N, Li T, Pugh EN Jr., Rux JJ, Speicher DW, and Pierce EA (2007). The proteome of the mouse photoreceptor sensory cilium complex. Mol Cell Proteomics 6, 1299–1317. 10.1074/mcp.M700054-MCP200. [PubMed: 17494944]

20. Venoux M, Delmouly K, Milhavet O, Vidal-Eychenie S, Giorgi D, and Rouquier S. (2008). Gene organization, evolution and expression of the microtubule-associated protein ASAP (MAP9). BMC Genomics 9, 406. 10.1186/1471-2164-9-406. [PubMed: 18782428]

21. Jensen VL, Carter S, Sanders AA, Li C, Kennedy J, Timbers TA, Cai J, Scheidel N, Kennedy BN, Morin RD, et al. (2016). Whole-Organism Developmental Expression Profiling Identifies RAB-28 as a Novel Ciliary GTPase Associated with the BBSome and Intraflagellar Transport. PLoS Genet 12, e1006469. 10.1371/journal.pgen.1006469.

22. Hao L, Thein M, Brust-Mascher I, Civelekoglu-Scholey G, Lu Y, Acar S, Prevo B, Shaham S, and Scholey JM (2011). Intraflagellar transport delivers tubulin isotypes to sensory cilium middle and distal segments. Nat Cell Biol 13, 790–798. 10.1038/ncb2268. [PubMed: 21642982]

23. Nishida K, Tsuchiya K, Obinata H, Onodera S, Honda Y, Lai YC, Haruta N, and Sugimoto A. (2021). Expression Patterns and Levels of All Tubulin Isotypes Analyzed in GFP Knock-In *C. elegans* Strains. Cell Struct Funct 46, 51–64. 10.1247/csf.21022. [PubMed: 33967119]

24. Garbrecht J, Laos T, Holzer E, Dillinger M, and Dammermann A. (2021). An acentriolar centrosome at the *C. elegans* ciliary base. Current biology : CB 31, 24182428 e2418. 10.1016/j.cub.2021.03.023.
25. Magescas J, Eskinazi S, Tran MV, and Feldman JL (2021). Centriole-less pericentriolar material serves as a microtubule organizing center at the base of *C. elegans* sensory cilia. Curr Biol 31, 2410–2417 e2416. 10.1016/j.cub.2021.03.022. [PubMed: 33798428]
26. Ward S, Thomson N, White JG, and Brenner S. (1975). Electron microscopical reconstruction of the anterior sensory anatomy of the nematode Caenorhabditis elegans.?2UU. J Comp Neurol 160, 313–337. 10.1002/cne.901600305. [PubMed: 1112927]
27. Perkins LA, Hedgecock EM, Thomson JN, and Culotti JG (1986). Mutant sensory cilia in the nematode Caenorhabditis elegans. Dev Biol 117, 456–487. 10.1016/0012-1606(86)90314-3. [PubMed: 2428682]
28. Li Y, Zhang Q, Wei Q, Zhang Y, Ling K, and Hu J. (2012). SUMOylation of the small GTPase ARL-13 promotes ciliary targeting of sensory receptors. J Cell Biol 199, 589–598. 10.1083/jcb.201203150. [PubMed: 23128241]
29. Cevik S, Sanders AA, Van Wijk E, Boldt K, Clarke L, van Reeuwijk J, Hori Y, Horn N, Hetterschijt L, Wdowicz A, et al. (2013). Active transport and diffusion barriers restrict Joubert Syndrome-associated ARL13B/ARL-13 to an Inv-like ciliary membrane subdomain. PLoS Genet 9, e1003977. 10.1371/journal.pgen.1003977.
30. Warburton-Pitt SR, Silva M, Nguyen KC, Hall DH, and Barr MM (2014). The nphp-2 and arl-13 genetic modules interact to regulate ciliogenesis and ciliary microtubule patterning in *C. elegans*. PLoS Genet 10, e1004866. 10.1371/journal.pgen.1004866.
31. Nechipurenko IV, Berciu C, Sengupta P, and Nicastro D. (2017). Centriolar remodeling underlies basal body maturation during ciliogenesis in Caenorhabditis elegans. Elife 6. 10.7554/eLife.25686.
32. Li W, Yi P, Zhu Z, Zhang X, Li W, and Ou G. (2017). Centriole translocation and degeneration during ciliogenesis in Caenorhabditis elegans neurons. The EMBO journal 36, 2553–2566. 10.15252/embj.201796883. [PubMed: 28743734]
33. Gadadhar S, Bodakuntla S, Natarajan K, and Janke C. (2017). The tubulin code at a glance. J Cell Sci 130, 1347–1353. 10.1242/jcs.199471. [PubMed: 28325758]
34. Wloga D, Joachimiak E, and Fabczak H. (2017). Tubulin Post-Translational Modifications and Microtubule Dynamics. Int J Mol Sci 18. 10.3390/ijms18102207.
35. Genova M, Grycova L, Puttrich V, Magiera MM, Lansky Z, Janke C, and Braun M. (2023). Tubulin polyglutamylation differentially regulates microtubule-interacting proteins. EMBO J 42, e112101. 10.15252/embj.2022112101. [PubMed: 36636822]
36. Mirvis M, Stearns T, and James Nelson W. (2018). Cilium structure, assembly, and disassembly regulated by the cytoskeleton. Biochem J 475, 2329–2353. 10.1042/BCJ20170453. [PubMed: 30064990]
37. Kimura Y, Kurabe N, Ikegami K, Tsutsumi K, Konishi Y, Kaplan OI, Kunitomo H, Iino Y, Blacque OE, and Setou M. (2010). Identification of tubulin deglutamylase among Caenorhabditis elegans and mammalian cytosolic carboxypeptidases (CCPs). J Biol Chem 285, 22936–22941. 10.1074/jbc.C110.128280. [PubMed: 20519502]
38. O'Hagan R, Silva M, Nguyen KCQ, Zhang W, Bellotti S, Ramadan YH, Hall DH, and Barr MM (2017). Glutamylation Regulates Transport, Specializes Function, and Sculpts the Structure of Cilia. Curr Biol 27, 3430–3441 e3436. 10.1016/j.cub.2017.09.066. [PubMed: 29129530]
39. Yu I, Garnham CP, and Roll-Mecak A. (2015). Writing and Reading the Tubulin Code. J Biol Chem 290, 17163–17172. 10.1074/jbc.R115.637447. [PubMed: 25957412]
40. Monroy BY, Tan TC, Oclaman JM, Han JS, Simo S, Niwa S, Nowakowski DW, McKenney RJ, and Ori-McKenney KM (2020). A Combinatorial MAP Code Dictates Polarized Microtubule Transport. Developmental cell 53, 60–72 e64. 10.1016/j.devcel.2020.01.029. [PubMed: 32109385]
41. Prevo B, Mangeol P, Oswald F, Scholey JM, and Peterman EJ (2015). Functional differentiation of cooperating kinesin-2 motors orchestrates cargo import and transport in *C. elegans* cilia. Nat Cell Biol 17, 1536–1545. 10.1038/ncb3263. [PubMed: 26523365]

42. Evans JE, Snow JJ, Gunnarson AL, Ou G, Stahlberg H, McDonald KL, and Scholey JM (2006). Functional modulation of IFT kinesins extends the sensory repertoire of ciliated neurons in Caenorhabditis elegans. J Cell Biol 172, 663–669. 10.1083/jcb.200509115. [PubMed: 16492809]
43. Lipton J, Kleemann G, Ghosh R, Lints R, and Emmons SW (2004). Mate searching in Caenorhabditis elegans: a genetic model for sex drive in a simple invertebrate. J Neurosci 24, 7427–7434. 10.1523/JNEUROSCI.1746-04.2004. [PubMed: 15329389]
44. Liu KS, and Sternberg PW (1995). Sensory regulation of male mating behavior in Caenorhabditis elegans. Neuron 14, 79–89. 10.1016/0896-6273(95)90242-2. [PubMed: 7826644]
45. Barr MM, and Sternberg PW (1999). A polycystic kidney-disease gene homologue required for male mating behaviour in *C. elegans*. Nature 401, 386–389. 10.1038/43913. [PubMed: 10517638]
46. Simon JM, and Sternberg PW (2002). Evidence of a mate-finding cue in the hermaphrodite nematode Caenorhabditis elegans. Proc Natl Acad Sci U S A 99, 1598–1603. 10.1073/pnas.032225799. [PubMed: 11818544]
47. Doroquez DB, Berciu C, Anderson JR, Sengupta P, and Nicastro D. (2014). A high-resolution morphological and ultrastructural map of anterior sensory cilia and glia in Caenorhabditis elegans. Elife 3, e01948. 10.7554/eLife.01948. [PubMed: 24668170]
48. Jumper J, Evans R, Pritzel A, Green T, Figurnov M, Ronneberger O, Tunyasuvunakool K, Bates R, Zidek A, Potapenko A, et al. (2021). Highly accurate protein structure prediction with AlphaFold. Nature 596, 583–589. 10.1038/s41586-021-03819-2. [PubMed: 34265844]
49. Varadi M, Anyango S, Deshpande M, Nair S, Natassia C, Yordanova G, Yuan D, Stroe O, Wood G, Laydon A, et al. (2022). AlphaFold Protein Structure Database: massively expanding the structural coverage of protein-sequence space with high-accuracy models. Nucleic Acids Res 50, D439–D444. 10.1093/nar/gkab1061. [PubMed: 34791371]
50. Kiesel P, Alvarez Viar G, Tsoy N, Maraspini R, Gorilak P, Varga V, Honigmann A, and Pigino G. (2020). The molecular structure of mammalian primary cilia revealed by cryo-electron tomography. Nat Struct Mol Biol 27, 1115–1124. 10.1038/s41594-020-0507-4. [PubMed: 32989303]
51. Gilliam JC, Chang JT, Sandoval IM, Zhang Y, Li T, Pittler SJ, Chiu W, and Wensel TG (2012). Three-dimensional architecture of the rod sensory cilium and its disruption in retinal neurodegeneration. Cell 151, 1029–1041. 10.1016/j.cell.2012.10.038. [PubMed: 23178122]
52. Konno A, Ikegami K, Konishi Y, Yang HJ, Abe M, Yamazaki M, Sakimura K, Yao I, Shiba K, Inaba K, and Setou M. (2016). Ttll9−/− mice sperm flagella show shortening of doublet 7, reduction of doublet 5 polyglutamylation and a stall in beating. J Cell Sci 129, 2757–2766. 10.1242/jcs.185983. [PubMed: 27257088]
53. Deane JA, Verghese E, Martelotto LG, Cain JE, Galtseva A, Rosenblum ND, Watkins DN, and Ricardo SD (2013). Visualizing renal primary cilia. Nephrology (Carlton) 18, 161–168. 10.1111/nep.12022. [PubMed: 23240784]
54. Moutin MJ, Bosc C, Peris L, and Andrieux A. (2021). Tubulin post-translational modifications control neuronal development and functions. Dev Neurobiol 81, 253–272. 10.1002/dneu.22774. [PubMed: 33325152]
55. Magiera MM, and Janke C. (2014). Post-translational modifications of tubulin. Curr Biol 24, R351–354. 10.1016/j.cub.2014.03.032. [PubMed: 24801181]
56. Edde B, Rossier J, Le Caer JP, Desbruyeres E, Gros F, and Denoulet P. (1990). Posttranslational glutamylation of alpha-tubulin. Science 247, 83–85. 10.1126/science.1967194. [PubMed: 1967194]
57. Viar GA, Klena N, Martino F, Nievergelt A, and Pigino G. (2023). The Tubulin Nano-Code: a protofilament-specific pattern of tubulin post-translational modifications regulates ciliary beating mechanics. bioRxiv, 2023.2006.2028.546853. 10.1101/2023.06.28.546853.
58. Khalifa AAZ, Ichikawa M, Dai D, Kubo S, Black CS, Peri K, McAlear TS, Veyron S, Yang SK, Vargas J, et al. (2020). The inner junction complex of the cilia is an interaction hub that involves tubulin post-translational modifications. Elife 9. 10.7554/eLife.52760.
59. Dymek EE, Lin J, Fu G, Porter ME, Nicastro D, and Smith EF (2019). PACRG and FAP20 form the inner junction of axonemal doublet microtubules and regulate ciliary motility. Mol Biol Cell 30, 1805–1816. 10.1091/mbc.E19-01-0063. [PubMed: 31116684]

60. Li Y, Wei Q, Zhang Y, Ling K, and Hu J. (2010). The small GTPases ARL-13 and ARL-3 coordinate intraflagellar transport and ciliogenesis. J Cell Biol 189, 1039–1051. 10.1083/jcb.200912001. [PubMed: 20530210]
61. Monroy BY, Sawyer DL, Ackermann BE, Borden MM, Tan TC, and Ori-McKenney KM (2018). Competition between microtubule-associated proteins directs motor transport. Nat Commun 9, 1487. 10.1038/s41467-018-03909-2. [PubMed: 29662074]
62. Dixit R, Ross JL, Goldman YE, and Holzbaur EL (2008). Differential regulation of dynein and kinesin motor proteins by tau. Science 319, 1086–1089. 10.1126/science.1152993. [PubMed: 18202255]
63. Lipka J, Kapitein LC, Jaworski J, and Hoogenraad CC (2016). Microtubule-binding protein doublecortin-like kinase 1 (DCLK1) guides kinesin-3-mediated cargo transport to dendrites. EMBO J 35, 302–318. 10.15252/embj.201592929. [PubMed: 26758546]
64. Ecklund KH, Morisaki T, Lammers LG, Marzo MG, Stasevich TJ, and Markus SM (2017). She1 affects dynein through direct interactions with the microtubule and the dynein microtubule-binding domain. Nat Commun 8, 2151. 10.1038/s41467-017-02004-2. [PubMed: 29247176]
65. Scholey JM (2013). Kinesin-2: a family of heterotrimeric and homodimeric motors with diverse intracellular transport functions. Annu Rev Cell Dev Biol 29, 443–469. 10.1146/annurev-cellbio-101512-122335. [PubMed: 23750925]
66. Zhang C, Han B, Guo Y, Guan H, Chen Z, Liu B, Sun W, Li W, Sun W, and Wang S. (2022). MAP9 Exhibits Protumor Activities and Immune Escape toward Bladder Cancer by Mediating TGF-beta1 Pathway. J Oncol 2022, 3778623. 10.1155/2022/3778623.
67. Wang S, Huang J, Li C, Zhao L, Wong CC, Zhai J, Zhou Y, Deng W, Zeng Y, Gao S, et al. (2020). MAP9 Loss Triggers Chromosomal Instability, Initiates Colorectal Tumorigenesis, and Is Associated with Poor Survival of Patients with Colorectal Cancer. Clin Cancer Res 26, 746–757. 10.1158/1078-0432.CCR-19-1611. [PubMed: 31662330]
68. Liu W, Xiao H, Wu S, Liu H, and Luo B. (2018). MAP9 single nucleotide polymorphism rs1058992 is a risk of EBV-associated gastric carcinoma in Chinese population. Acta Virol 62, 435–440. 10.4149/av_2018_412. [PubMed: 30472874]
69. Dickinson DJ, Ward JD, Reiner DJ, and Goldstein B. (2013). Engineering the Caenorhabditis elegans genome using Cas9-triggered homologous recombination. Nat Methods 10, 1028–1034. 10.1038/nmeth.2641. [PubMed: 23995389]
70. Dickinson DJ, Pani AM, Heppert JK, Higgins CD, and Goldstein B. (2015). Streamlined Genome Engineering with a Self-Excising Drug Selection Cassette. Genetics 200, 1035–1049. 10.1534/genetics.115.178335. [PubMed: 26044593]
71. Sallee MD, Zonka JC, Skokan TD, Raftrey BC, and Feldman JL (2018). Tissue-specific degradation of essential centrosome components reveals distinct microtubule populations at microtubule organizing centers. PLoS Biol 16, e2005189. 10.1371/journal.pbio.2005189.
72. Mangeol P, Prevo B, and Peterman EJ (2016). KymographClear and KymographDirect: two tools for the automated quantitative analysis of molecular and cellular dynamics using kymographs. Mol Biol Cell 27, 1948–1957. 10.1091/mbc.E15-060404. [PubMed: 27099372]
73. Sulston JE, and Brenner S. (1974). The DNA of Caenorhabditis elegans. Genetics 77, 95–104. 10.1093/genetics/77.1.95. [PubMed: 4858229]
74. Siahaan V, Tan R, Humhalova T, Libusova L, Lacey SE, Tan T, Dacy M, Ori-McKenney KM, McKenney RJ, Braun M, and Lansky Z. (2022). Microtubule lattice spacing governs cohesive envelope formation of tau family proteins. Nat Chem Biol 18, 1224–1235. 10.1038/s41589-022-01096-2. [PubMed: 35996000]
75. Fink G, Hajdo L, Skowronek KJ, Reuther C, Kasprzak AA, and Diez S. (2009). The mitotic kinesin-14 Ncd drives directional microtubule-microtubule sliding. Nat Cell Biol 11, 717–723. 10.1038/ncb1877. [PubMed: 19430467]
76. Walther P, and Ziegler A. (2002). Freeze substitution of high-pressure frozen samples: the visibility of biological membranes is improved when the substitution medium contains water. J Microsc 208, 3–10. 10.1046/j.1365-2818.2002.01064.x. [PubMed: 12366592]

77. Buser C, and Walther P. (2008). Freeze-substitution: the addition of water to polar solvents enhances the retention of structure and acts at temperatures around −60 degrees C. J Microsc 230, 268–277. 10.1111/j.1365-2818.2008.01984.x. [PubMed: 18445157]

78. Sato T. (1968). A modified method for lead staining of thin sections. J Electron Microsc (Tokyo) 17, 158–159. [PubMed: 4177281]

79. Kremer JR, Mastronarde DN, and McIntosh JR (1996). Computer visualization of three-dimensional image data using IMOD. J Struct Biol 116, 71–76. 10.1006/jsbi.1996.0013. [PubMed: 8742726]

80. Schindelin J, Arganda-Carreras I, Frise E, Kaynig V, Longair M, Pietzsch T, Preibisch S, Rueden C, Saalfeld S, Schmid B, et al. (2012). Fiji: an open-source platform for biological-image analysis. Nat Methods 9, 676–682. 10.1038/nmeth.2019. [PubMed: 22743772]

81. Laine RF, Tosheva KL, Gustafsson N, Gray RDM, Almada P, Albrecht D, Risa GT, Hurtig F, Lindas AC, Baum B, et al. (2019). NanoJ: a high-performance open- source super-resolution microscopy toolbox. J Phys D Appl Phys 52, 163001. 10.1088/1361-6463/ab0261.

82. Edgar RC (2004). MUSCLE: a multiple sequence alignment method with reduced time and space complexity. BMC Bioinformatics 5, 113. 10.1186/1471-2105-5-113. [PubMed: 15318951]

83. Waterhouse AM, Procter JB, Martin DM, Clamp M, and Barton GJ (2009). Jalview Version 2--a multiple sequence alignment editor and analysis workbench. Bioinformatics 25, 1189–1191. 10.1093/bioinformatics/btp033. [PubMed: 19151095]

84. Guindon S, Dufayard JF, Lefort V, Anisimova M, Hordijk W, and Gascuel O. (2010). New algorithms and methods to estimate maximum-likelihood phylogenies: assessing the performance of PhyML 3.0. Syst Biol 59, 307–321. 10.1093/sysbio/syq010. [PubMed: 20525638]

85. Lefort V, Longueville JE, and Gascuel O. (2017). SMS: Smart Model Selection in PhyML. Mol Biol Evol 34, 2422–2424. 10.1093/molbev/msx149. [PubMed: 28472384]

86. Arshadi C, Gunther U, Eddison M, Harrington KIS, and Ferreira TA (2021). SNT: a unifying toolbox for quantification of neuronal anatomy. Nat Methods 18, 374–377. 10.1038/s41592-021-01105-7. [PubMed: 33795878]

87. Snow JJ, Ou G, Gunnarson AL, Walker MR, Zhou HM, Brust-Mascher I, and Scholey JM (2004). Two anterograde intraflagellar transport motors cooperate to build sensory cilia on *C. elegans* neurons. Nat Cell Biol 6, 1109–1113. 10.1038/ncb1186. [PubMed: 15489852]

88. Mukhopadhyay S, Lu Y, Qin H, Lanjuin A, Shaham S, and Sengupta P. (2007). Distinct IFT mechanisms contribute to the generation of ciliary structural diversity in *C. elegans*. EMBO J 26, 2966–2980. 10.1038/sj.emboj.7601717. [PubMed: 17510633]

Highlights

- *C. elegans* MAPH-9 localizes exclusively to microtubule doublets (MTDs)
- MAPH-9 localization is in part mediated by tubulin polyglutamylation
- *maph-9* deletion perturbs MTD ultrastructure, motor movement, and cilia function
- MAP9 is conserved in metazoans and localizes to the proximal cilium in mammals

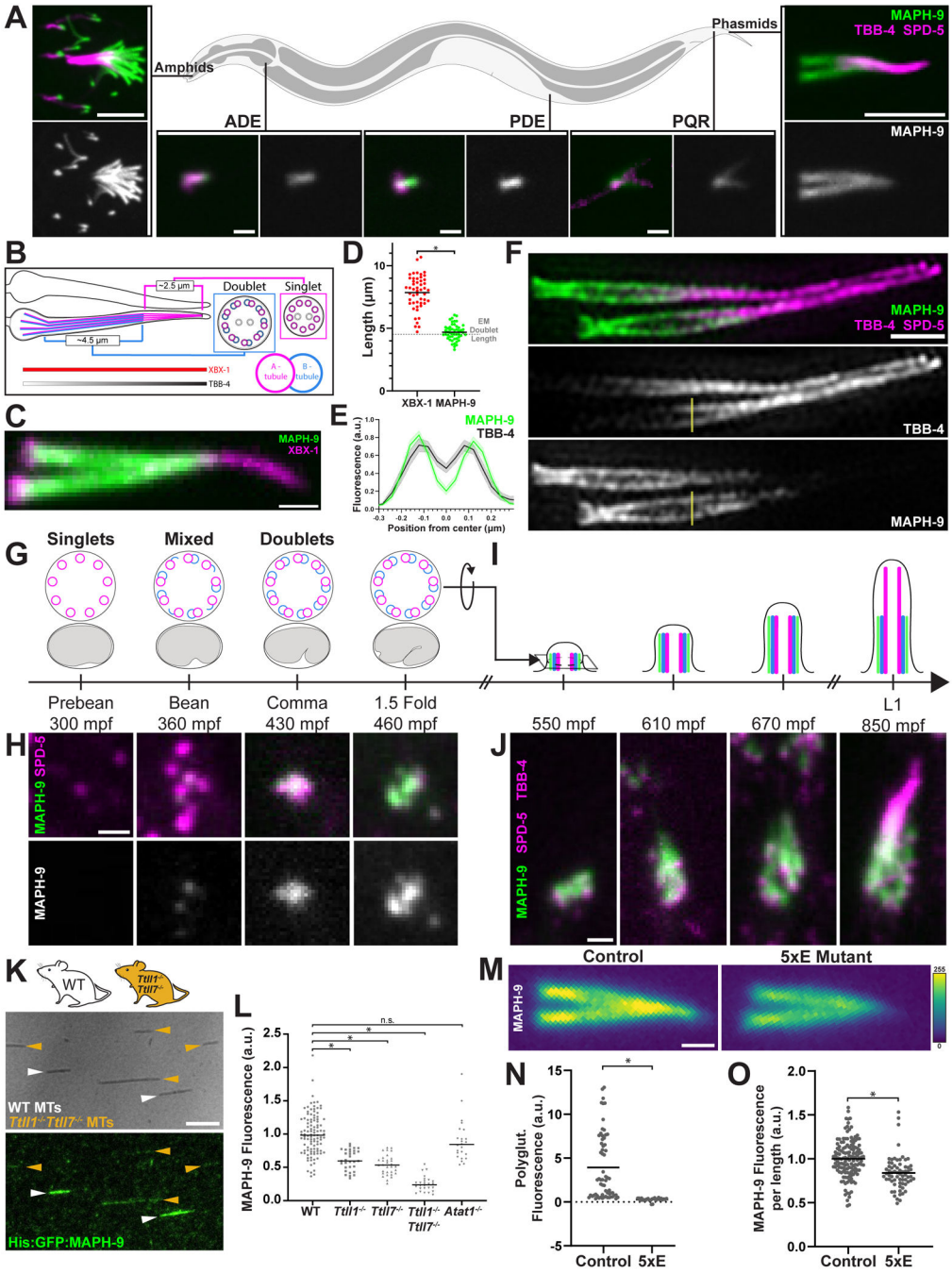

Figure 1. MAPH-9 localizes to microtubule doublets and preferentially binds polyglutamylated microtubules

(A) Endogenously tagged GFP::MAPH-9 (green), TBB-4::RFP, and RFP::SPD-5 (magenta) in indicated ciliated sensory neurons in adult worms. TBB-4/SPD-5 brightness scaled differently in PQR. Scale bars: Amphids and Phasmids, 5 µm; ADE, PDE, PQR, 1 µm.

(B) Schematic depicting phasmid axoneme structure. Cross section in the doublet or singlet region with the A-tubule (magenta) and B-tubule (blue) indicated.

(C) Localization of endogenous GFP::MAPH-9 (green) and XBX-1::RFP (magenta) in adult phasmid cilia. Scale bar, 1 µm.

(D) Quantification of protein localization length (μm) from ciliary base marked by XBX-1. Dashed horizontal line is MTD length from EM in amphid cilia (~4.5 μm). XBX-1: 7.86±1.33 n=50; MAPH-9: 4.69±0.63 n=50; $p<0.0001$.
(E) Averaged line profiles of MAPH-9 (green) and TBB-4 (black) fluorescence (a.u.) drawn perpendicular to the middle segment of the axoneme in 3D SIM imaging (yellow line on 1F): MAPH-9: 0.35±0.062 μm n=16; TBB-4: 0.30±0.036 μm n=13. $p<0.05$
(F) 3D structured illumination imaging of endogenous GFP::MAPH-9 (green) and TBB-4::RFP/RFP::SPD-5 (magenta) in adult phasmid cilia. Scale bar, 1 μm.
(G) Schematic depicting the timeline of MTD development at centrioles (top, cross-sectional view) in amphid neurons during *C. elegans* embryonic development (bottom, side view) at indicated minutes post-fertilization (m.p.f.)[31].
(H) Localization of endogenous GFP::MAPH-9 (green) and RFP::SPD-5 (magenta) in amphid neurons through embryonic development. Scale bar, 1 μm.
(I) Longitudinal view schematic depicting A-tubule (magenta), B-tubule (blue), and MAPH-9 (green) localization during amphid ciliogenesis in the embryo at indicated m.p.f.
(J) Localization of endogenous GFP::MAPH-9 (green) and RFP::SPD-5/TBB-4::RFP (magenta) during ciliogenesis in amphids. Scale bar, 1 μm.
(K) Total Internal Reflection Fluorescence microscopy images of: Top: microtubules assembled from tubulin from wild-type (WT) mice (white arrowheads) or $Ttll1^{-/-}$ and $Ttll7^{-/-}$ mice (orange arrowheads); Bottom: MAPH-9 localization. Scale bar, 5 μm.
(L) Quantification of normalized fluorescence intensity of MAPH-9 localized to microtubules assembled from tubulin extracted from mice with indicated genotypes. WT: 1.0±0.31 n=105; $Ttll1^{-/-}$: 0.61±0.15 n=31 $p<0.0001$; $Ttll7^{-/-}$: 0.54±0.15 n=31 $p<.0001$; $Ttll1^{-/-}$ $Ttll7^{-/-}$: 0.25±0.11 n=26 $p<0.0001$; $Atat1^{-/-}$: 0.89±.31 n=24 $p=0.15$.
(M) Heat map localization of endogenous GFP::MAPH-9 in phasmid cilia in Control and *ttll-4(tm3310), ttll-5(tm4059), ttll-9(tm3889), ttll-11(tm3360), tll-15(tm3871)* polyglutamylation mutant (5xE mutant). Scale bar, 1 μm.
(N) Quantification of fluorescence of α-polyglutamylated tubulin (GT335 antibody) staining. Control: 3.94±3.79 n=63; 5xE mutant: 0.28±0.19 n=25 $p<0.0001$.
(O) Quantification of MAPH-9 fluorescence per unit length normalized to Control. Control:1±0.211 n=140; 5XE:0.83±0.19 n=68 $p<0.0001$.
Values are mean±SD. p-values are calculated by Student's t-test and represent a comparison to Control. Graphs present individual data points with horizontal bar representing the mean.

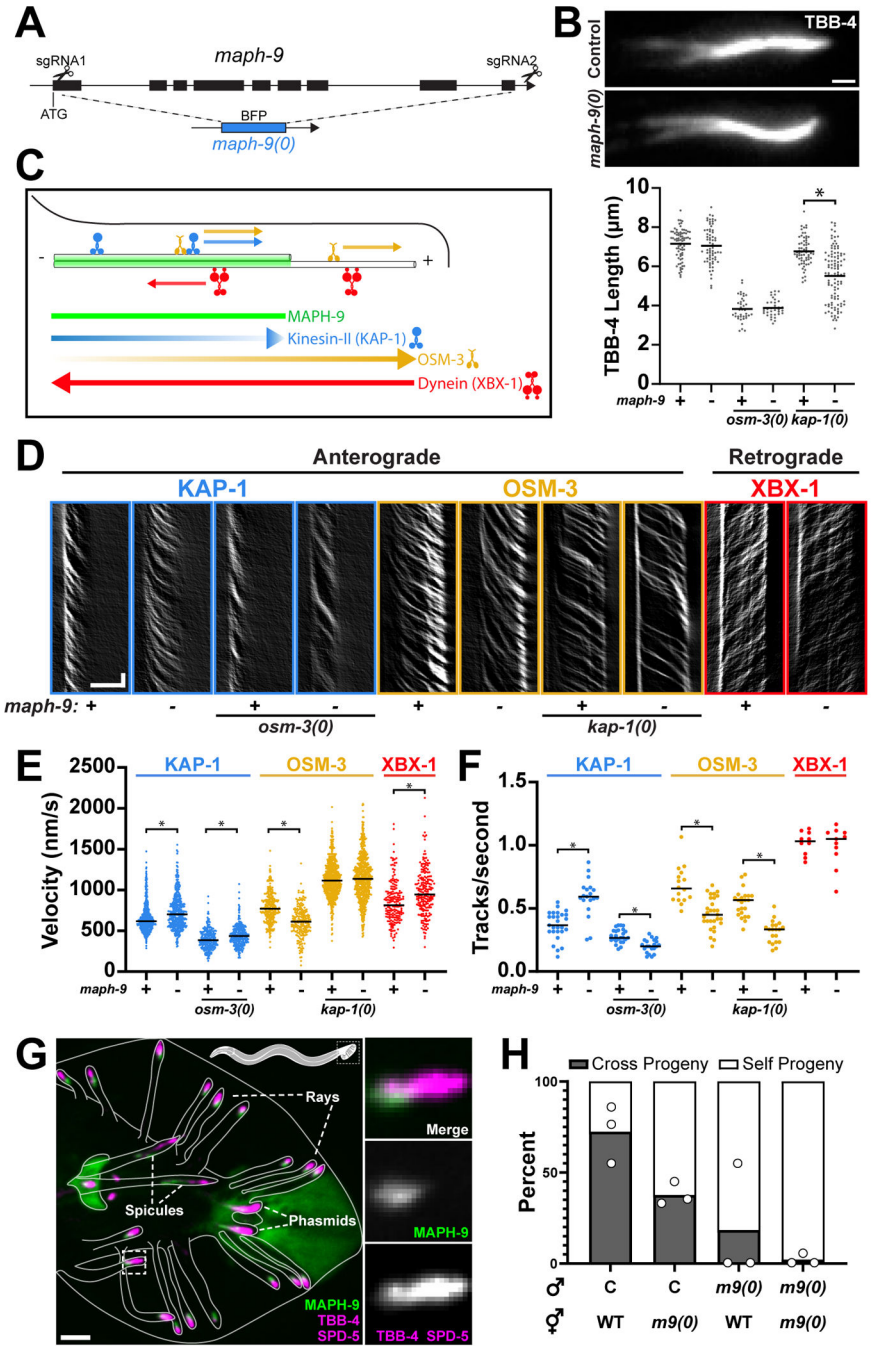

Figure 2. MAPH-9 modulates motor speed and promotes cilia function

(A) Schematic of endogenous *maph-9* locus with sgRNA cut sites and BFP (blue fluorescent protein) replacement indicated to make *maph-9(0)* mutant allele.

(B) Top: Localization of endogenous TBB-4::RFP in Control and *maph-9(0)* mutant. Scale bar, 1 µm. Bottom: Quantification of TBB-4 fluorescence length (µm). Control: 7.15±0.76 n=76. *maph-9(0)*:7.05±0.93 n=67. *osm-3(0)*: 3.82±0.61 n=38. *osm-3(0)*; *maph-9(0)*:3.88±0.42 n=36. *kap-1(0)*:6.73±0.78 n=66. *kap-1(0)*; *maph-9(0)*:5.51±1.34 n=106. *: p<0.0001

(C) Schematic depicting ciliary motors on the axoneme. Colored bars and arrows depict protein localization and direction of movement (anterograde to the right, retrograde to the left) in a *C. elegans* cilium.

(D) Representative kymographs of KAP-1, OSM-3, and XBX-1 in Control, *maph-9(0)* (‘*m9(0)*’) mutant, or other indicated mutant backgrounds. Scale bar, 5 μm (x); 1s (y).

(E) Quantification of motor velocity (nm/s). KAP-1::GFP [Control: 655.4±169.7 n=614. *maph-9(0)*: 731.9±206.3 n=478; *osm-3(0)*: 397.6±120.9 n=289; *osm-3(0)*; *maph-9(0)*: 440.9±128.7 n=287]; OSM-3::GFP [Control: 781.9±181.7 n=319; *maph-9(0)*: 609.1±186.7 n=217; *kap-1(0)*: 1128.4±216.5 n=765; *kap-1(0)*; *maph-9(0)*: 1128.4±280.4 n=673]; XBX-1::RFP [Control: 850.8±255.8 n=177; *maph-9(0)*: 973.4±282.0 n=203]. *: p<0.0001

(F) Quantification of number of motors/second. KAP-1::GFP [Control: 0.367±0.11 n=27; *maph-9(0)*: 0.588±0.152 n=19; *osm-3(0)*: 0.28±.054 n=25; *osm-3(0)*; *maph-9(0)*: 0.202±0.052 n=21]; OSM-3::GFP [Control: 0.682±0.15 n=16; *maph-9(0)*: 0.459±0.12 n=29; *kap-1(0)*: 0.541±0.108 n=23; *kap-1(0)*; *maph-9(0)*: 0.316±0.088 n=20]; XBX-1::RFP [Control: 1.02±0.0917 n=10; *maph-9(0)*: 0.996±0.157 n=11]. *: p<0.0001

(G) Localization of endogenous GFP::MAPH-9 (green) and RFP::SPD-5, TBB-4::RFP (magenta) in an adult male tail. Right Insets display endogenous GFP::MAPH-9 localization in the cilium of an individual ray. Scale bar, 5 μm.

(H) Mating efficiency: Quantification of percent of progeny from mating (cross-progeny) or from self-progeny with wild-type (‘WT’) or *maph-9(0)* (‘*m9(0)*’) mutant or Control (‘C’) worms as indicated (Male x Hermaphrodite): Control x wild-type: 65±12.49% n=3; Control x *maph-9(0)*: 33±5.69% n=3; *maph-9(0)* x wild-type: 16±28.29% n=3; *maph-9(0)* x *maph-9(0)*: 2±3.46% n=3

Values are mean±SD. p-values are calculated by Student’s t-test. Graphs present individual data points with horizontal bar representing the mean.

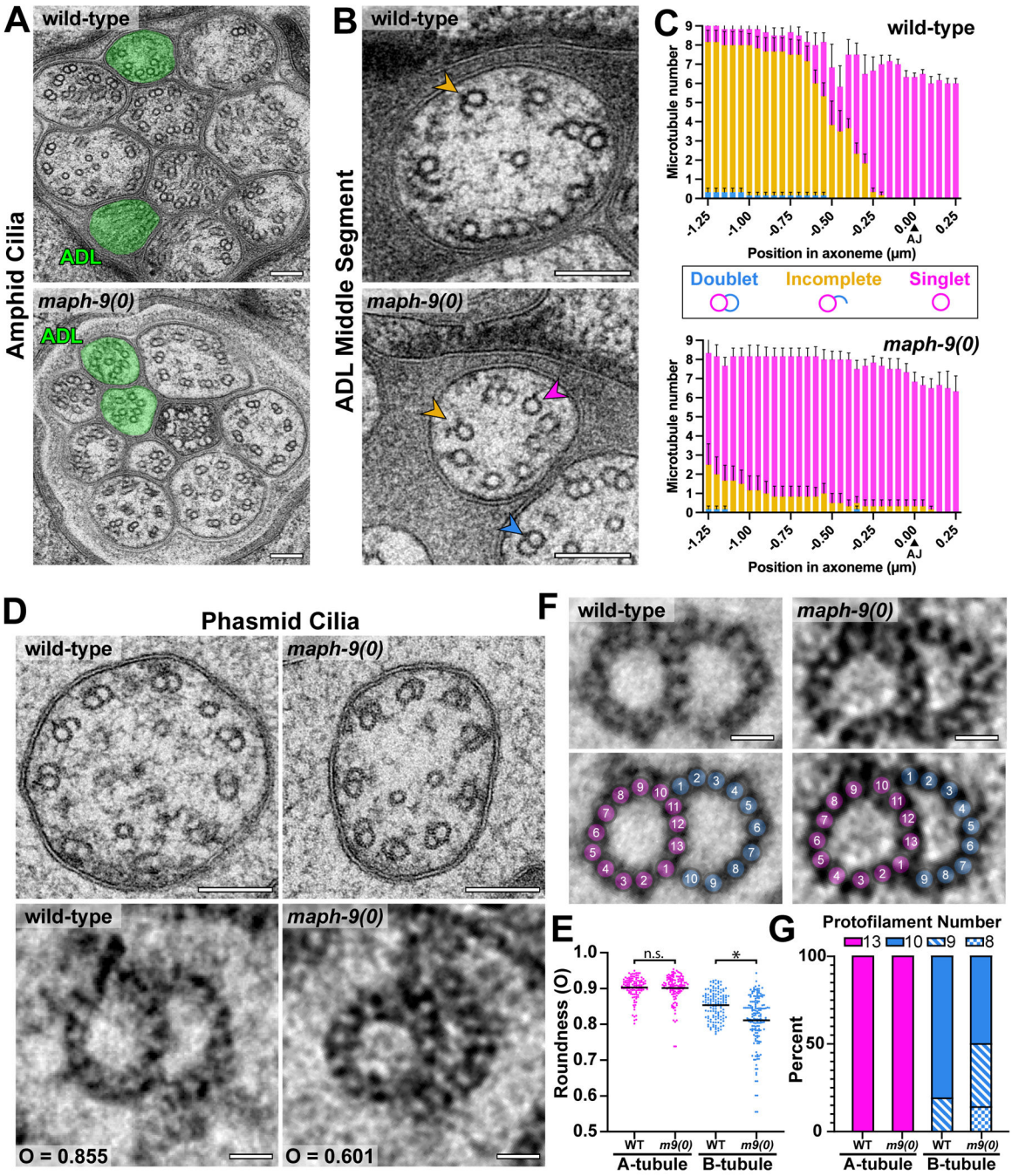

Figure 3. Loss of *MAPH-9 causes ultrastructural microtubule doublet defects in the axoneme*

(A) Representative electron microscopy (EM) images of amphid middle segment axonemes in wild-type and *maph-9(0)* mutant worms with ADL neurons indicated in green. Scale bar, 100 nm.

(B) Representative EM images of amphid ADL neuron axonemes in indicated genotype. Arrowheads indicate representative singlet (magenta) or incomplete doublet (orange) microtubule in ADL and non-ADL MTD (blue). Scale bar, 100 nm.

(C) Quantification of MTD (blue), incomplete doublets (orange), and singlet (magenta) microtubules in ADL axonemes in sections in the middle segment going proximal (left) to distal (right). Sections were aligned (0 position) using the autojunction (AJ) of the amphid socket. Control: 3 ADL neurons, 6 cilia, 2 worms, n = 1408 microtubules; *maph-9(0)*: 3 ADL 6 cilia, 2 worms, n =1431 microtubules.

(D) Top: Representative EM images of cross sections through adult phasmid neurons of indicated genotypes. Scale bar, 100 nm.

Bottom: Examples of individual phasmid MTDs with genotype and roundness measurement (O) indicated. Scale bar, 10 nm.

(E) Roundness measurement (O) of MTDs in wild-type and maph-9(0) mutant phasmid axonemes: A-tubule [wild-type ('WT'): 0.903±0.03; maph-9(0) ('m9(0)'): 0.902±0.037 $p>0.05$]; B-tubule [wild-type: 0.85±0.04; maph-9(0): 0.81±0.07 $p<0.001$]; wild-type n=3 worms,148 sections; maph-9(0) n=4 worms, 305 sections.

(F) Representative phasmid MTD from indicated genotype (top) with protofilaments labeled (bottom).

(G) Quantification of protofilament (PF) number: A-tubule [wild-type: 13PF – 100% n=37; *maph-9(0)*: 13PF – 100% n=50]; B-tubule [wild-type: 10PF – 81% 9PF – 19% n=37; *maph-9(0)*: 10PF – 50% 9PF – 36%; 8PF – 14% n =50]. B-tubule average [wild-type: 9.81; *maph-9(0)*: 9.36 $p<0.001$]

Values are mean±SEM. p-values are calculated by Student's t-test.

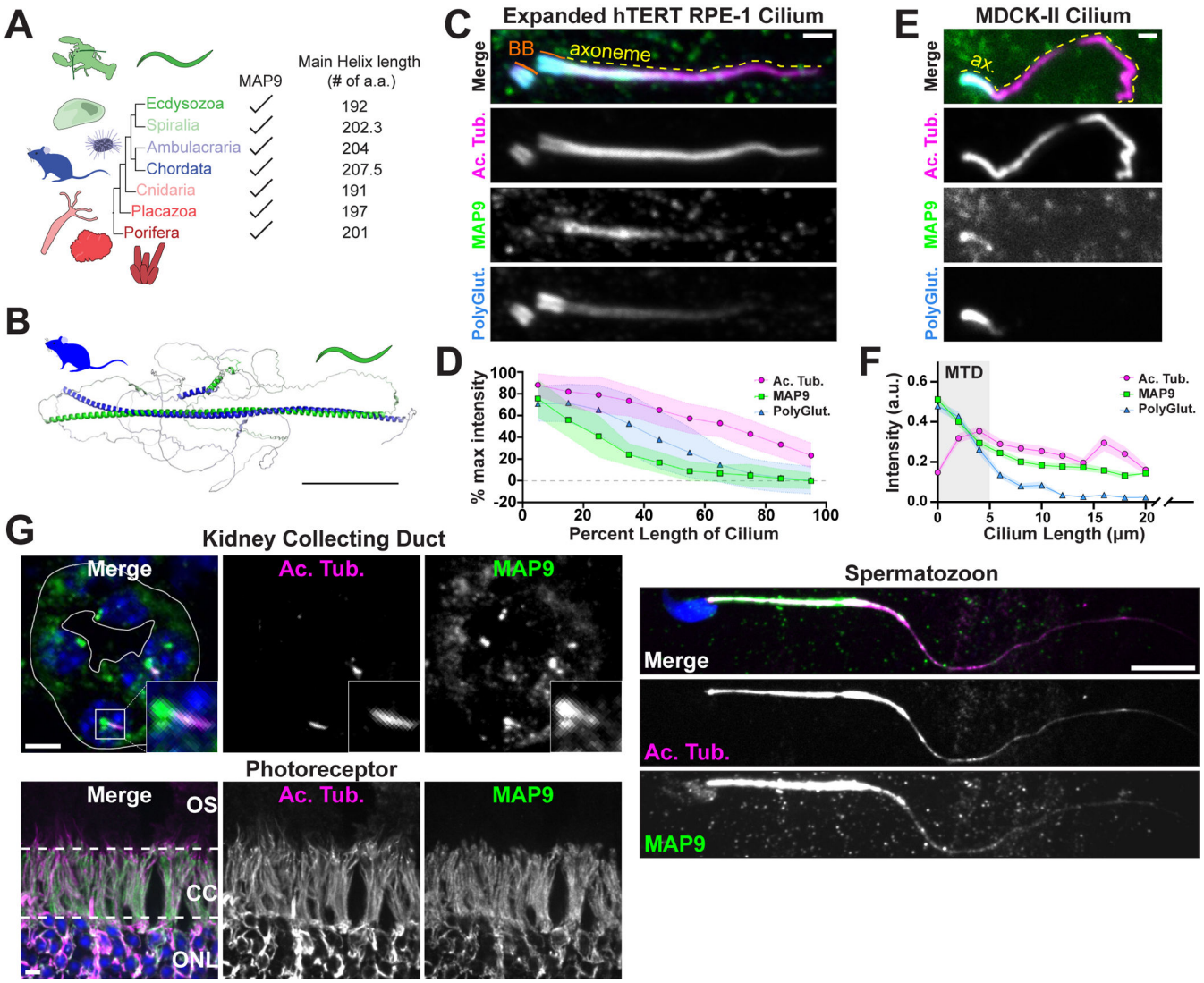

Figure 4. MAP9 localization is conserved in mammalian cells

(A) MAP9 homologs with a consistent main alpha-helix length are present throughout Metazoa.

(B) Aligned AlphaFold structural predictions for mouse MAP9 (blue) and *C. elegans* MAPH-9 (green) Scale bar, 100Å. Root mean square deviation = 9.390.

(C) Isotropically expanded hTERT RPE-1 cell stained with antibodies against MAP9 (green), acetylated tubulin (‘Ac. Tub.’, magenta), and polyglutamylated tubulin (‘PolyGlut.’, cyan). Basal bodies (BB, orange) and axoneme (yellow dashed line) indicated in merge. Note that MAP9 localizes to the proximal axoneme and dimly to the basal bodies. Scale bar, 1 μm.

(D) Percent of max fluorescence of background subtracted MAP9, polyglutamylated tubulin, and acetylated tubulin binned by percent of the cilium length determined by acetylated tubulin staining in hTERT RPE-1 cells (n=18). Error bars = standard deviation from the mean.

(E) MDCK-II cell cultured using the same protocol as for existing MDCK-II MTD measurement[50] stained with indicated antibodies. Axoneme ('ax.', yellow dashed line) indicated in merge. Scale bar, 1 μm.

(F) Percent of max fluorescence of MAP9, polyglutamylated tubulin, and acetylated tubulin binned by cilium length determined by acetylated tubulin staining in MDCK-II cells (n=87). Error bars = 95% confidence interval. Grey box represents MTD region previously observed by EM50 with B-tubules variably terminating between ~2–5 μm. Note that the x-axis has been cropped to 20 μm.

(G) Indicated mouse tissues fixed and stained with antibodies against MAP9 (green), acetylated tubulin (magenta), and DAPI (blue). Kidney collecting duct: Scale bar, 5 μm. Eye photoreceptor: outer segment (OS) connecting cilium (CC) outer nuclear layer (ONL). Scale bar, 5 μm. Spermatozoon: Scale bar, 10 μm.

Key resources table

REAGENT or RESOURCE	SOURCE	IDENTIFIER
Antibodies		
anti-centrin 20H5	Sigma-Aldrich	04–1624; RRID: AB_10563501
anti-polyglutamylated tubulin GT335	AdipoGen	20B0020C100; RRID: AB_2490210
anti-acetylated tubulin 6–11B-1	Sigma-Aldrich	T6793; RRID: AB_2819178
anti-MAP9	Proteintech	26078–1-AP; RRID: AB_2880366
anti-MAP9	invitrogen	PA5–58145; RRID: AB_2643755
anti-GFP	Roche	11814460001; RRID: AB_390913
anti-alpha-tubulin	Sigma-Aldrich	T6199; RRID: AB_477583
anti-mouse IgG1 – 568	Thermo Fischer Scientific	A-21124; RRID: AB_2535766
Anti-mouse IgG1 – 488	Thermo Fischer Scientific	A-21121; RRID: AB_2535764
anti-mouse IgG1 – 647	Thermo Fisher Scientific	A-21240; RRID: AB_2535809
anti-mouse IgG2a – 647	Thermo Fischer Scientific	A-21241; RRID: AB_2535810
anti-mouse IgG2a – 568	Thermo Fischer Scientific	A-21134; RRID: AB_2535773
anti-mouse IgG2b – 488	Thermo Fischer Scientific	A-21141; RRID: AB_2535778
anti-mouse IgG2b – 568	Thermo Fisher Scientific	A-21144; RRID: AB_2535780
anti-rabbit IgG – 568	Thermo Fisher Scientific	A-11036; RRID: AB_10563566
anti-rabbit IgG – 488	Thermo Fischer Scientific	A-11034; RRID: AB_2576217
anti-mouse IgG – 680	Li-COR Biosciences	926–68071; RRID: AB_10956166
anti-rabbit IgG – 800	Li-COR Biosciences	926–32211; RRID: AB_621843
DAPI	Thermo Fischer Scientific	D1306
DAPI	Vector Laboratories	H-2000
anti-biotin antibody solution	Sigma-Aldrich	B3640; RRID: AB_258552
anti-tubulin	Sigma-Aldrich	T7816–2ML; RRID: AB_261770
Bacterial and virus strains		
E. coli OP50	Caenorhabditis Genetics Center	NA
E. coli HT115 RNAi bacteria	Caenorhabditis Genetics Center	NA
E. coli BL21 DE3	Sigma-Aldrich	CMC0014
Chemicals, peptides, and recombinant proteins		
Ampicillin Sodium Salt	Thermo Fisher Scientific	BP1760
Cosmic Calf Serum	HyClone	SH30087.04
DiI (1,1′-dioctadecyl-3,3,3′, 3′-tetramethylindocarbocyanine perchlorate)	Medchemexpress	HY-D0083

REAGENT or RESOURCE	SOURCE	IDENTIFIER
DMEM F12 (1:1)	Gibco	11330–032
DMEM with 4.5g/L glucose, L-glut, sodium pyruvate	Corning	10–013-CV
GMPCPP	Jena Bioscience	NU-405
Halt Protease Inhibitor Cocktail	Thermo Fisher Scientific	78430
Horse Serum	Thermo Fisher Scientific	16050–122
Isopropyl-β-D-thiogalactopyranoside (IPTG)	Thermo Fisher Scientific	BP175510
Levamisole hydrochloride	Sigma-Aldrich	Cat#31742
Mowiol® 4–88	EMD Millipore	475904–100GM
N,N′-Methylenebisacrylamide solution	Sigma-Aldrich	M1533
Ni-NTA Agarose	Invitrogen	R90115
nitrocellulose membrane	Bio-Rad	162–0112
Normal Goat Serum	Jackson Immuno Research	005–000-121
Pluronic F127	Sigma-Aldrich	P2443
Ponceau S solution	Sigma-Aldrich	P7170
Scigen Tissue-Plus™ OCT Compound	Fisher Scientific	23–730-571
Sodium Acrylate	Sigma-Aldrich	408220
Trypsin 0.25%	Corning	25–053-CI
Critical commercial assays		
Q5 Site-Directed Mutagenesis Kit	New England Biolabs	Cat#E05548
NEBuilder HiFi DNA Assembly	New England Biolabs	Cat#E5520S
lipofectamine 3000	Invitrogen	L3000015
Experimental models: Cell lines		
Human: hTERT RPE-1	ATCC	CRL-4000; RRID:CVCL_4388
Dog: MDCK-II	Gift from James Nelson	N/A
Experimental models: Organisms/strains		
C. elegans: JLF1105: spd-5(wow36[tagrfp-t::3xmyc::spd-5]) I; maph-9(wow95[zf::gfp::3xflag::maph-9]) IV; tbb-4(wow150[tbb-4::rfp])X	This Study	N/A
C. elegans: JLF999: maph-9(wow95[zf::gfp::3xflag::maph-9]) IV; xbx-1(cas502[xbx-1::tagrfp-t::3xmyc]) V	This Study	N/A
C. elegans: JLF1525: ttll-4(tm3310) III; maph-9(wow197[zf::gfp::3xflag::maph-9]) IV; ttll-11(tm4059) IV; ttll-15(tm3871)V; ttll-5(tm3360) V; ttll-9(tm3889) V	This Study	N/A
C. elegans: JLF1439: him-9(e1487) II; maph-9(wow95[zf::gfp::3xflag::maph-9]) IV	This Study	N/A
C. elegans: JLF1427: spd-5(wow36[tagrfp-t::3xmyc::spd-5]) I; maph-9(wow95[zf::gfp::3xflag::maph-9]) IV; wowEx161(maph-9P::myrBFP::unc-54UTR)	This Study	N/A
C. elegans: PD1074		N/A
C. elegans: JLF625: maph-9(wow105[maph-9p::bfp+maph-9 UTR]) IV	This Study	N/A
C. elegans: JLF1405: spd-5(wow53[zf::gfp::3xflag::spd-5]) I; him-5(e1490) V; tbb-4(wow150[tbb-4::rfp]) X	This Study	N/A

REAGENT or RESOURCE	SOURCE	IDENTIFIER
C. elegans: JLF1406: spd-5(wow53[zf::gfp::3xflag::spd-5]) I; maph-9(wow105[maph-9p::bfp+maph-9 UTR]) IV; him-5(e1490) V; tbb-4(wow150[tbb-4::rfp]) X	This Study	N/A
C. elegans: JLF1106: spd-5(wow36[tagrfp-t::3xmyc::spd-5]) I; kap-1(ok676) III; maph-9(wow105[maph-9p::bfp+maph-9 UTR]) IV; tbb-4(wow150[tbb-4::rfp]) X	This Study	N/A
C. elegans: JLF1268: spd-5(wow36[tagrfp-t::3xmyc::spd-5]) I; kap-1(ok676) III; maph-9(wow95[zf::gfp::3xflag::maph-9]) IV; tbb-4(wow150[tbb-4::rfp]) X	This Study	N/A
C. elegans: JLF1423: spd-5(wow36[tagrfp-t::3xmyc::spd-5]) I; osm-3(p802) IV; tbb-4(wow150[tbb-4::rfp]) X	This Study	N/A
C. elegans: JLF1104: spd-5(wow36[tagrfp-t::3xmyc::spd-5]) I; osm-3(p802) IV; maph-9(wow105[maph-9p::bfp+maph-9 UTR]) IV; tbb-4(wow150[tbb-4::rfp]) X	This Study	N/A
C. elegans: JLF1521: kap-1(wow196[kap-1::GFP] III	This Study	N/A
C. elegans: JLF1522: kap-1(wow196[kap-1::GFP] III; maph-9(wow105[maph-9p::bfp+maph-9 UTR]) IV	This Study	N/A
C. elegans: JLF1523: kap-1(wow196[kap-1::GFP] III; osm-3(p802) IV	This Study	N/A
C. elegans: JLF1524: kap-1(wow196[kap-1::GFP] III; osm-3(p802) IV; maph-9(wow105[maph-9p::bfp+maph-9 UTR]) IV	This Study	N/A
C. elegans: JLF1321: osm-3(wow171[osm-3::GFP] IV	This Study	N/A
C. elegans: JLF1322: osm-3(wow171[osm-3::GFP] IV; maph-9(wow105[maph-9p::bfp+maph-9 UTR]) IV	This Study	N/A
C. elegans: JLF1407: kap-1(ok676) III; osm-3(wow171[osm-3::GFP]) IV	This Study	N/A
C. elegans: JLF1408: kap-1(ok676) III; osm-3(wow171[osm-3::GFP]) IV; maph-9(wow105[maph-9p::bfp+maph-9 UTR]) IV	This Study	N/A
C. elegans: JLF999: maph-9(wow95[zf::gfp::3xflag::maph-9]) IV; xbx-1(cas502[xbx-1::tagRFP])V	This Study	N/A
C. elegans: JLF670: maph-9(wow105[maph-9p::bfp+maph-9 UTR]) IV; xbx-1(cas502[xbx-1::tagRFP]) V	This Study	N/A
C. elegans: JLF1405: spd-5(wow53[zf::gfp::3xflag::spd-5]) I; him-5(e1490) V; tbb-4(wow150[tbb-4::rfp]) X	This Study	N/A
C. elegans: JLF1406: spd-5(wow53[zf::gfp::3xflag::spd-5]) I; maph-9(wow105[maph-9p::bfp+maph-9 UTR]) IV; him-5(e1490) V; tbb-4(wow150[tbb-4::rfp]) X	This Study	N/A
C. elegans: JLF1407: kap-1(ok676) III; osm-3(wow171[osm-3::GFP] IV	This Study	N/A
C. elegans: JLF1408: kap-1(ok676) III; osm-3(wow171[osm-3::GFP] IV; maph-9(wow105[maph-9p::bfp+maph-9 UTR]) IV	This Study	N/A
C. elegans: JLF767: tba-5(wow134[tba-5:GFP]) I; xbx-1(cas502[xbx-1::tagrfp-t::3xmyc]) V	This Study	N/A
C. elegans: JLF768: tba-5(wow134[tba-5:GFP]) I; maph-9(wow105[maph-9p::bfp+maph-9 UTR]) IV; xbx-1(cas502[xbx-1::tagrfp-t::3xmyc]) V	This Study	N/A
C. elegans: JLF1106: spd-5(wow36[tagrfp-t::3xmyc::spd-5]) I; kap-1(ok676) III; tbb-4(wow150[tbb-4::rfp]) X	This Study	N/A
C. elegans: JLF1206: wowSi15jsSi1671[elt-2p::nuclear GFP] II; him-5(e1490) V	This Study	N/A
C. elegans: JLF1207: wowSi15jsSi1671[elt-2p::nuclear GFP] II; maph-9(wow105) IV; him-5(e1490) V	This Study	N/A
C. elegans: JLF1545: arl13(wow198[arl13:gfp]) I;maph-9(wow155[rfp:maph-9]) IV	This Study	N/A

REAGENT or RESOURCE	SOURCE	IDENTIFIER
C. elegans: JLF1423: spd-5(wow36[tagrfp-t::3xmyc::spd-5]) I; osm-3(p802) IV; maph-9(wow95[zf::gfp::3xflag::maph-9]) IV; tbb-4(wow150[tbb-4::rfp]) X	This Study	N/A
C. elegans: JLF1268: spd-5(wow36[tagrfp-t::3xmyc::spd-5]) I; kap-1(ok676) III; maph-9(wow105[maph-9p::bfp+maph-9 UTR]) IV; tbb-4(wow150[tbb-4::rfp]) X	This Study	N/A
C. elegans: JLF1104: spd-5(wow36[tagrfp-t::3xmyc::spd-5]) I; osm-3(p802) IV; maph-9(wow105[maph-9p::bfp+maph-9 UTR]) IV; tbb-4(wow150[tbb-4::rfp]) X	This Study	N/A
Oligonucleotides		
CRISPR targeting sequence (+PAM): maph-9(wow105[maph-9p::bfp+maph-9 UTR]) IV: TGCACATATGTATTACATT(CGG)	This Study	N/A
CRISPR targeting sequence (+PAM): maph-9(wow105[maph-9p::bfp+maph-9 UTR]) IV: AACGATCGAGAAGTCGTCC(TGG)	This Study	N/A
CRISPR targeting sequence (+PAM): tbb-4(wow150[tbb-4::tagrfp-t::3xmyc]) X: TGATGAGCACGATCAAGATG(TGG)	This Study	N/A
CRISPR targeting sequence (+PAM): tba-5(wow134[tba-5::gfp:3xflag]) I: TCCTAATATTCTTCATCATT(TGG)	This Study	N/A
CRISPR targeting sequence (+PAM): osm-3(wow171[osm-3::gfp::3xflag]: GAATTATTTGGGATTCAGAG(AGG)	This Study	N/A
CRISPR targeting sequence (+PAM): maph-9(wow186[zf::gfp::3xflag::maph-9]: ccaacatgttccagtgaaAT(GGG)	This Study	N/A
CRISPR targeting sequence (+PAM): arl-13(wow150[arl-13::gfp:3xflag]) I: GCTTCAAAAGTGAAAAA(AGG)	This Study	N/A
CRISPR targeting sequence (+PAM): kap-1(wow196[kap-1::gfp:3xflag]) III ACAAACAAAAGTTAAAAAAG(GGG)	This Study	N/A
CRISPR targeting sequence (+PAM): maph-9(wow155[tagrfp-t::3xmyc::MAPH-9]) IV ccaacatgttccagtgaaAT(GGG)	This Study	N/A
Primers for CRISPR edits, see Table S2		
Recombinant DNA		
Plasmid pJJR81: BFP Empty Repair Template	Gift from Mike Boxem	Addgene plasmid # 75029; RRID: Addgene_75029
Plasmid pDD162: Peft-3::Cas9 + Empty sgRNA	Dickenson et al.[69]	Addgene plasmid # 47549; RRID:Addgene_47549
Plasmid pDD282: GFP^SEC^3xFlag vector with ccdB markers for cloning homology arms	Dickenson et al.[70]	Addgene plasmid # 66823; RRID: Addgene_66823
Plasmid pDD286: TagRFP-T^SEC^3xMyc vector with ccdB sites for cloning homology arms	Gift from Bob Goldstein	Addgene plasmid # 70684; RRID: Addgene_70684
Plasmid pET His6 GFP TEV LIC cloning vector	Gift from Scott Gradia	Addgene plasmid # 29663; RRID: Addgene_29663
Plasmid pJF250: ZF::GFP::3xFlag Empty repair template	Sallee et al.[71]	N/A
Plasmid pEGFP-N1: CMVp:GFP	clontech	Plasmid #6085–1
Plasmid pMT2: Peft-3::Cas9 + maph-9 sgRNA	Magescas et al.[25]	N/A
Plasmid pMT3: ZF::GFP::3xFlag maph-9 repair template	Magescas et al.[25]	N/A
Plasmid pMT5: BFP maph-9 Repair template	this study	N/A
Plasmid pMT6: eft-3p::Cas9 + maph-9 5'UTR sgRNA	this study	N/A
Plasmid pMT7: eft-3p::Cas9 + maph-9 3' sgRNA	this study	N/A

REAGENT or RESOURCE	SOURCE	IDENTIFIER
Plasmid pMT8: His6:GFP:TEV:maph-9	this study	N/A
Plasmid pMT9: CMVp:GFP:MAP9	this study	N/A
Plasmid pMT10: CMVp:GFP:MAPH-9	this study	N/A
Plasmid pMT11: Peft-3::cas9 + kap-1 sgRNA	this study	N/A
Plasmid pMT12: GFP::3xFlag kap-1 repair template	this study	N/A
Plasmid pMT13: tagRFP-T::3xmyc maph-9 repair template	this study	N/A
Plasmid pJM74: Pmaph-9::myr::tagBFP2::unc-54UTR	Magescas et al.[25]	N/A
Plasmid pJM58: Peft-3::cas9 + tba-5 sgRNA	this study	N/A
Plasmid pJM60: GFP::3xFLag tba-5 repair template	this study	N/A
Plasmid pJM80: Peft-3::cas9 + osm-3 sgRNA	this study	N/A
Plasmid pJM81: GFP::3xFlag osm-3 repair template	this study	N/A
Plasmid pJM56: Peft-3::cas9 + tbb-4 sgRNA	this study	N/A
Plasmid pJM57: tagRFP-T::3xmyc tbb-4 repair template	this study	N/A
Plasmid pJM72: Peft-3::cas9 + arl-13 sgRNA	this study	N/A
Plasmid pJM73: GFP::3xFlag arl-13 repair template	this study	N/A
Software and algorithms		
Fiji/ImageJ (version 1.53)	NIH	RRID: SCR_002285
Prism for Windows (version 9.3.1)	GraphPad	RRID: SCR_002798
NIS elements	Nikon Instruments	RRID: SCR_014329
Excel	Microsoft	RRID: SCR_016137
Photoshop	Adobe	RRID: SCR_014199
Illustrator	Adobe	RRID: SCR_010279
Indesign	Adobe	RRID: SCR_021799
KymographClear 2.0	Mangeol, P., et al.[72]	N/A
KymographDirect 2.0	Mangeol, P., et al.[72]	N/A
AlphaFold v2	DeepMind	RRID: SCR_023662
JalView	Geoff Barton's Group at the University of Dundee	RRID: SCR_006459
PhyML 3.0	ATGC: Montpellier Bioinformatics platform	RRID: SCR_014629